PROCESS PARAMETER OPTIMIZATION OF ADDITIVELY MANUFACTURED MARAGING STEEL

A Thesis Submitted to
the Graduate School of
İzmir Institute of Technology
in Partial Fulfillment of the Requirements for the Degree of

MASTER OF SCIENCE

in Mechanical Engineering

by
Burak SİVRİ

July 2024
İZMİR

We approve the thesis of **Burak SİVRİ**

Examining Committee Members:

Prof. Dr. H. Seçil ARTEM
Mechanical Engineering, İzmir Institute of Technology

Assist. Prof. Dr. Halil TETİK
Mechanical Engineering, İzmir Institute of Technology

Prof. Dr. B. Burak ÖZHAN
Mechanical Engineering, Manisa Celal Bayar University

5 / July / 2024

Prof. Dr. H. Seçil ARTEM
Mechanical Engineering,
İzmir Institute of Technology

Prof. Dr. M. İ. Can DEDE
Head of the Department of
Mechanical Engineering,
İzmir Institute of Technology

Prof. Dr. Mehtap EANES
Dean of the Graduate School,
İzmir Institute of Technology

ACKNOWLEDGEMENTS

I would like to express my endless gratitude to my academic supervisor, Prof. Dr. H. Seçil Artem. She has been a constant source of encouragement throughout my thesis study. Prof. Artem's guidance, patience and motivation has been invaluable, and I am deeply grateful for her willingness to share her knowledge and expertise with me. I will always be proud to have worked with Prof. Artem, and I cherish the opportunity to learn from such a dedicated and knowledgeable mentor.

I would like to thank Sinan Nuri Nane, Çetin Bakıcı and Dr. Emre Ak for their help and encouragement. I would also like to thank Hayri Altıntaş for his support.

I should state that I am grateful to my mother, Nilgün Sivri and my father, Mehmet Sivri who have always encouraged me along this way. Furthermore, I offer sincere thanks to my girlfriend Kübra Nur Ulukaya, for the support she has provided in this difficult journey.

Lastly, I would like to thank everyone who helped me, both directly and indirectly. Your support and assistance have been invaluable, and I am deeply grateful for your contributions.

ABSTRACT

PROCESS PARAMETER OPTIMIZATION OF ADDITIVELY MANUFACTURED MARAGING STEEL

This study investigates additive manufacturing parameters of maraging steel parts using laser powder bed fusion. Laser powder bed fusion can be used to quickly manufacture lightweight and strong parts but requires precise calibration of process parameters such as laser power, scanning speed and layer thickness. Maintaining a good compatibility between these factors is important and the ability to predict the part quality is essential due to this method's complexity and cost. Maraging steel is known for its high strength, hardness and ductility. During additive manufacturing, maraging steel constantly undergoes a phase change from austenite to martensite, due to the constant cooling and heating cycles caused by layer-by-layer manufacturing.

This thesis aims to utilize a phase-changing maraging steel material model, create finite element analyses of laser powder bed fusion and employ direct optimization methods to introduce artificial factors to the analyses to align the finite element model to yield consistent results with the physical tests from literature. Then, metamodel of optimal prognosis from the simulation and experiment data is created. Stochastic optimization methods are discussed, and an evolutionary algorithm is trained with the metamodel of optimal prognosis to predict parameter compatibility and identify optimal manufacturing parameters.

This thesis prioritizes deflection caused by the residual effects of metal additive manufacturing as the main failure output of the optimization problem. The findings demonstrated that, despite hardships, near residual effect free maraging steel parts could be additively manufactured by utilizing simulation and optimization methods. A method for increasing the accuracy and efficiency of additive manufacturing of maraging steel is proposed, highlighting the benefits of finite element analysis and stochastic optimization methods.

Keywords: *Laser Powder Bed Fusion, Additive Manufacturing, Maraging Steel, Finite Element Analysis, Stochastic Optimization, Evolutionary Algorithm, Thermomechanical Simulation*

ÖZET

EKLEMELİ İMALATLA ÜRETİLEN MARAŞLAMA ÇELİĞİNİN PROSES PARAMETRE OPTİMİZASYONU

Bu çalışmada lazer toz yatak füzyonu ile üretilen maraşlama çeliği parçaların üretim parametleri araştırılmaktadır. Lazer toz yatak füzyonu, hafif ve mukavim parçaların hızlı üretilmesini sağlar ancak lazer gücü, tarama hızı ve katman kalınlığı gibi proses parametrelerinin hassas bir şekilde kalibre edilmesi gerekmektedir. Üretim yönteminin karmaşıklığı ve maliyetleri nedeniyle parametreler arası uyumun ve parça kalitesinin öngörülebilir olması kritiktir. Maraşlama çeliği yüksek mukavemet, sertlik ve süneklik gibi mekanik özelliklere sahiptir. Maraşlama çeliği, metal eklemeli imalat esnasında gerçekleşen katmanlı üretim nedeniyle peş peşe ısınma ve soğuma döngülerine maruz kalır ve süreç boyunca östenit ve martenzit fazları arasında geçiş yapar.

Bu çalışma, içerisinde faz dönüşümü bilgisi içeren bir maraşlame çeliği malzeme modelini kullanmayı, lazer toz yatağı füzyonunun sonlu elemanlar analizini oluşturmayı, analize yapay faktörler ekleyerek analiz modelini literatürden alınan fiziksel test sonuçlarıyla uyumlu çıktılar verecek şekilde direkt optimizasyon metotlarıyla kalibre etmeyi içermektedir. Sonrasında ise simülasyon ve literatür çıktıları ile optimum öngörü sağlayacak bir metamodel oluşturulmaktadır. Stokastik optimizasyon metotları incelendikten sonra evrimsel bir algoritma metamodel verisi ile eğitilmekte, üretim parametreleri arası uyum ve ideal eklemeli imalat parametreleri elde edilmektedir.

Bu araştırmada üretim sebebiyle oluşan deformasyon başlıca optimizasyon problemi olarak belirlenmiştir ve bu etkinin minimuma indirgenmesi hedeflenmiştir. Araştırmada elde edilen bulgular, maraşlama çeliğinin simülasyon ve optimizasyon metotları sayesinde sıfıra yakın deformasyon ile üretilebileceğini göstermektedir. Bu çalışmada maraşlama çeliği eklemeli imalatının doğruluğunu ve verimliliğini artırmak adına bir yöntem önerilmekte olup, bu doğrultuda sonlu elemanlar analizi ve optimizasyon yöntemlerinin faydaları vurgulanmaktadır.

Anahtar Kelimeler: *Lazer Toz Yatağı Füzyonu, Eklemeli İmalat, Maraşlama Çeliği, Sonlu Elemanlar Analizi, Stokastik Optimizasyon, Evrimsel Algoritma, Termomekanik Simülasyon*

TABLE OF CONTENTS

LIST OF FIGURES

Figure **Page**

LIST OF TABLES

Table **Page**

CHAPTER 1

INTRODUCTION

This chapter provides an introduction to additive manufacturing of maraging steel, laser powder bed fusion simulation and optimization methods. In this chapter, objective of this thesis is explained along with a literature review.

1.1. Literature Survey

By enabling distributed manufacturing and the production of parts-on-demand, additive manufacturing—also known as direct digital manufacturing, free form fabrication, 3D printing, etc.—a rapidly evolving manufacturing technology possesses the potential to completely change the global parts manufacturing and logistics industry while also possibly reducing costs, energy consumption, and carbon footprint (Frazier 2014).

Complex metallic 3D components can be manufactured with the widely utilized metal additive manufacturing method referred to as laser powder bed fusion (L-PBF). One of the metals utilized in additive manufacturing (AM) is maraging steel, a material that is a member of the class of ultra-high-strength steels used in the tooling and aerospace industries even though its microstructure and mechanical characteristics require post-AM thermal treatment (Kizhakkinan et al. 2023).

Numerical simulation developed specifically for additive manufacturing offers a viable alternative for producing metallic parts through AM, particularly when it comes to process parameter optimization for minimizing residual stress and preventing cracks or distortion in the final parts. This can help reduce the significant time and cost associated with AM studies (Chen 2019). The significance of numerical simulation in additive manufacturing lies in its capacity to effectively and precisely predict and analyse complex physical phenomena such as heat and mass transfer and microstructure evolution. This makes it an important instrument for picking process parameters in metal additive manufacturing (Gao et al. 2021).

Scan speed, laser power, and hatch distance are some of the most essential variables in the L-PBF process given that they can combine to produce broad

solidification techniques that have significant effects on the mechanical properties of the printed parts (Cacace and Semeraro 2022). The residual stress in additively built components is influenced by build process parameters, like energy beam power and movement speed, which have been extensively studied in the L-PBF (W. Zhang et al. 2022). Similar parameters are utilized as such in numerical simulations of AM such as finite element analysis (FEA).

The most significant process variables that either directly or indirectly impact the L-PBF process are layer thickness, scanning speed, laser power, and hatch distance. Specifically, it is also known that the shape and melt pool formation are controlled by laser power and scanning speed. For all these reasons, it is often necessary to recharacterize the information. Therefore, it's critical to create techniques that cut down on the time and expense required to define a trustworthy set of process parameters. The process of determining the ideal set of process parameters requires thorough specimen analysis to ensure that the material is fully dense and free of processing-related defects. Typically, this involves printing a large number of specimens and analysing them later to assess the material density and potential presence of defects (Giorgetti et al. 2023). Thus, combined with the fact that sample manufacturing can be costly, optimization methods are used to fine-tune parameters in AM.

AM Process optimization involves numerically characterising a process in an organized manner and then identifying the best machine configuration and process parameters to meet specific objectives. A high-quality item is primarily dependent on having optimal process parameters during the printing process. To properly optimize a process, a number of parameters and the consequent geometric and physical qualities need to be taken into account. In metal AM research, machine learning (ML) technologies are being employed more and more to handle the intricate interplay between parameters and properties (Roberts, Xia, and Kennedy 2022). Machine learning, evolutionary algorithms, and genetic algorithms are being applied increasingly in additive manufacturing to improve various aspects of the process, from optimization and quality control to novel design approaches.

For a variety of applications, additive manufacturing is actively involving machine learning (ML) models. In laser-based metal additive manufacturing methods, machine learning techniques are applied to detect defects, providing additional channels for immediate process and quality control (Herzog et al. 2024). In order to drive the next generation of additive manufacturing by obtaining improved process efficiency and

material quality, more developments in machine learning models investigate process-dependent material evolution (Parsazadeh, Sharma, and Dahotre 2023).

Evolutionary and genetic algorithms are branches of machine learning, inspired from natural selection. Evolutionary algorithms have demonstrated the ability to optimize additive manufacturing process factors, such as scheduling and design optimization, to increase the effectiveness of the process and the quality of printed components (Leirmo and Martinsen 2019). On the other hand, genetic algorithms are especially helpful in resolving intricate optimization issues in additive manufacturing. They have been used to cut operational expenses and lead to optimized production capacity (Castillo-Rivera et al. 2020).

Finite element analysis plays a crucial role in metal additive manufacturing as it can provide insights into the structural performance of manufactured parts, but also can make use of machine learning, evolutionary and genetic algorithms. Engineers may design more dependable and efficient parts by using simulation to forecast how structures will respond to various loads and stress conditions (Castellazzi et al. 2015). Additive manufacturing gains from improved design validation, optimized metal parts for particular applications, and the capacity to anticipate and deal with possible manufacturing problems prior to production through the use of FEA. When FEA and metal AM work together, manufacturing efficiency is increased, material waste is decreased, and components that are both structurally sound and customized to meet particular user requirements are produced.

This study focuses on numerically investigating the AM process of maraging steel, making use of data from existing publications, thermal and structural FEA, direct and stochastic optimization methods, in order to present a solid solution towards fault free metal additive manufacturing of maraging steel.

1.2. Objectives of the Study

Laser powder bed fusion additive manufacturing can create lightweight and strong metal parts very quickly. However, several factors, such as laser power, scanning speed, layer thickness, and part quality, must be carefully calibrated in order to produce high-quality parts. Predicting these characteristics' compatibility and the quality of the final product is crucial due to the production method's complexity and cost. Usually, finite

element simulations of the additive manufacturing process, test part printing, and simulation software calibration using physical outcomes are used to reach this forecast. This way, successful prints can be made without having to pay high manufacturing expenses.

Maraging steel, which has a reputation for having exceptional strength and hardness, is frequently utilized in vital components that demand these qualities and can be used in additive manufacturing. The components that compose this alloy include iron, nickel, and cobalt along with titanium, aluminium, and molybdenum. Maraging steel is used in industrial environments where high strength and ductility are necessary. As it cools during the metal additive manufacturing process, maraging steel transitions from austenite to martensite. Predicting the behaviour of the material during manufacturing requires a thorough simulation of this phase change (ANSYS 2024).

Based on the literature review, manufacturing high quality maraging steel parts via metal additive manufacturing is difficult and expensive due to the necessity of good compatibility between manufacturing parameters and phase change characteristics of the material during simulation. Design of experiment studies or trainable optimization algorithms could be conducted to predict the results of this complex process. So, in order to print quality maraging steel parts with ease, the aim of this thesis carries the following objectives:

1) Utilizing a phase changing material model from literature and finding physical experiment results of a benchmark maraging steel laser powder bed fusion part.
2) Making use of direct optimization to calibrate the phase changing material model and finite element analysis so physical and numerical additive manufacturing processes produce consistent results.
3) Training a stochastic optimization algorithm with the calibrated numerical simulation models.
4) Having the trained algorithm predict compatibility of different parameters and suggest parameters combinations for manufacturing.
5) Identification of optimum manufacturing parameter combinations for laser powder bed fusion of maraging steel.

CHAPTER 2

ADDITIVE MANUFACTURING

This chapter investigates the archetypes of additive manufacturing along with a clear definition of what AM is. Several methods and classifications of AM are discussed and established, followed by a deeper understanding of metal additive manufacturing (MAM) and MAM types. This chapter also investigates the parameters used in MAM and how they affect the printed part. Moreover, subjects such as residual stresses and MAM part failures are discussed.

2.1. Additive Manufacturing

Today's highly competitive global market demands that manufacturers concentrate on delivering high-quality goods quickly, effectively, and affordably if they wish to witness their manufacturing processes succeed. Global competitiveness is greatly aided by additive manufacturing, sometimes referred to as 3D printing, layer-wise manufacturing, rapid prototyping/manufacturing, or solid free-form fabrication (Mugwagwa and Dimitrov 2019).

A variety of technologies are referred to as additive manufacturing because they can convert virtual solid model data into physical models through an automated process. The information is divided into a set of finite-thickness 2D cross-sections. These cross-sections are put into additive manufacturing machines, where they are formed, assembled, and combined layer by layer to make the physical part. As a result, the AM machine replicates the digital part's geometry physically without requiring any modifications for manufacturing processes, such as tooling, undercuts, draft angles, or other features (Gibson et al. 2020). This method is more effective than traditional methods of manufacturing such as drilling, milling, and casting. Considered an energy and material-efficient technique, 3D printing can save up to 50% of energy while using up to 90% of resources (Kantaros, Ganetsos, and Piromalis 2023).

From being limited to quick prototyping in the late 1980s, additive manufacturing has grown in importance over time for low-volume end-use component manufacturing. The processing of metals and composites, as well as quality enhancement, have become

more important since the year 2000 (Mugwagwa and Dimitrov 2019). A chart of revenue rise for AM can be found in Figure 2.1.

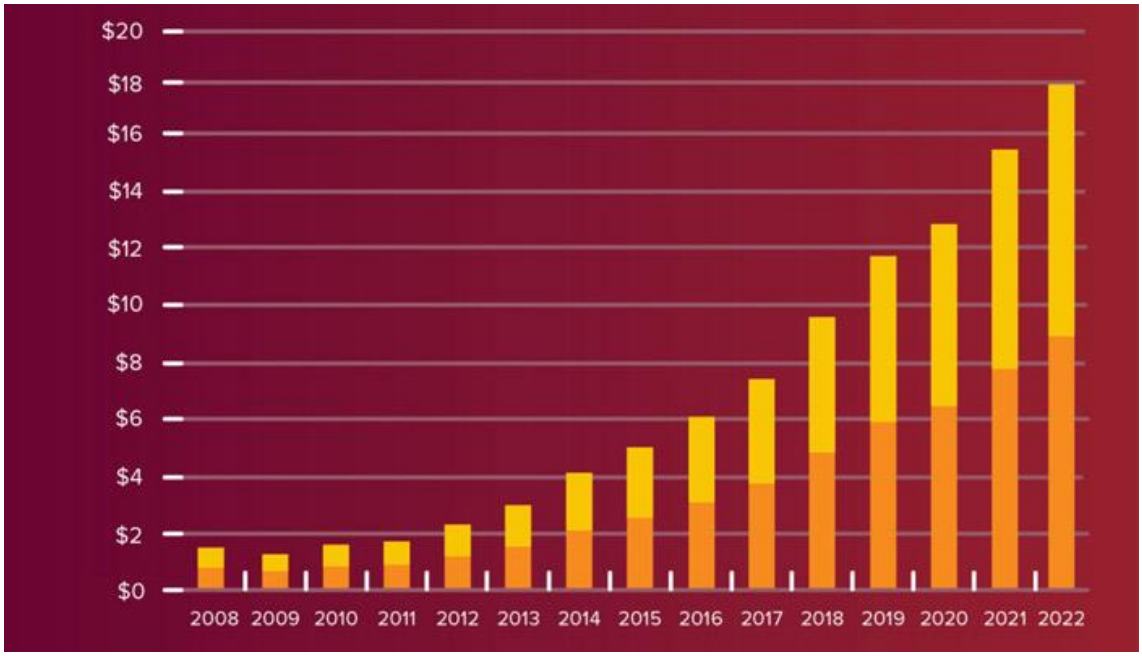

Figure 2.1. Rise in revenue for AM services between 2008 and 2022
(Source: Wohlers et al. 2023)

There are now a number of additive manufacturing techniques available; they vary in terms of the materials that can be utilized, the operating principle, and the way layers are deposited to build things. Certain techniques, such as selective laser melting (SLM), selective laser sintering (SLS), and fused deposition modeling (FDM), cure liquid materials, yet other techniques, such as stereolithography (SLA), melt or soften materials in order to generate layers. Because each approach has benefits as well as disadvantages of its own, some manufacturers provide an option between powder and polymer for the substance that the object is made of (Bikas, Stavropoulos, and Chryssolouris 2016).

2.1.1. Extrusion Based Processes

In order to soften or melt material—typically plastic—provided in the form of wire, thermal material extrusion techniques employ a heated extrusion nozzle. When the material has melted, it is deposited through an extrusion nozzle and allowed to cool before

solidifying to form the final part geometry (Bikas, Stavropoulos, and Chryssolouris 2016).

2.1.1.1 Fused Deposition Modeling

A moveable head is used in the FDM process to deposit a thread of molten thermoplastic material onto a substrate. A simple schematic explaining the deposition process can be found in Figure 2.2.

In order for the material to solidify immediately after extrusion and subsequently weld to the preceding layers, it is heated to a temperature that is 1°C over its melting point (Chryssolouris G 2005).

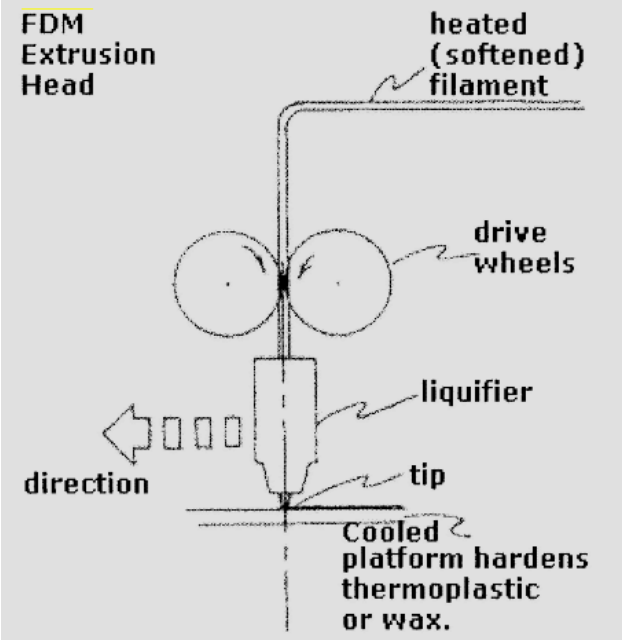

Figure 2.2. Filament deposition process (Source: Chryssolouris G 2005)

2.1.1.2 Robocasting

Robocasting is a freeform production method based on layer-wise deposition of heavily loaded colloidal slurries for thick ceramics and composites. Parts of the process can be manufactured, dried, and fully sintered in less than 24 hours, and it is essentially binderless with less than 1% organic material (Cesarano, King, and Denham n.d.).

2.1.2. Material Jetting

Using material jetting (MJ) technology, functional parts can be built by selectively curing liquid photopolymer. Air-excluding tanks are used in MJ to hold photopolymer ingredients, which are then heated in the transmission line that transfers photopolymer from tank to nozzle and deposited as droplets that form an extremely thin layer on the build platform. On the build platform, molten material is exposed to ultraviolet (UV) radiation for curing, which causes the material to solidify (Gülcan, Günaydın, and Tamer 2021). A simple schematic explaining the material jetting process can be found in Figure 2.3.

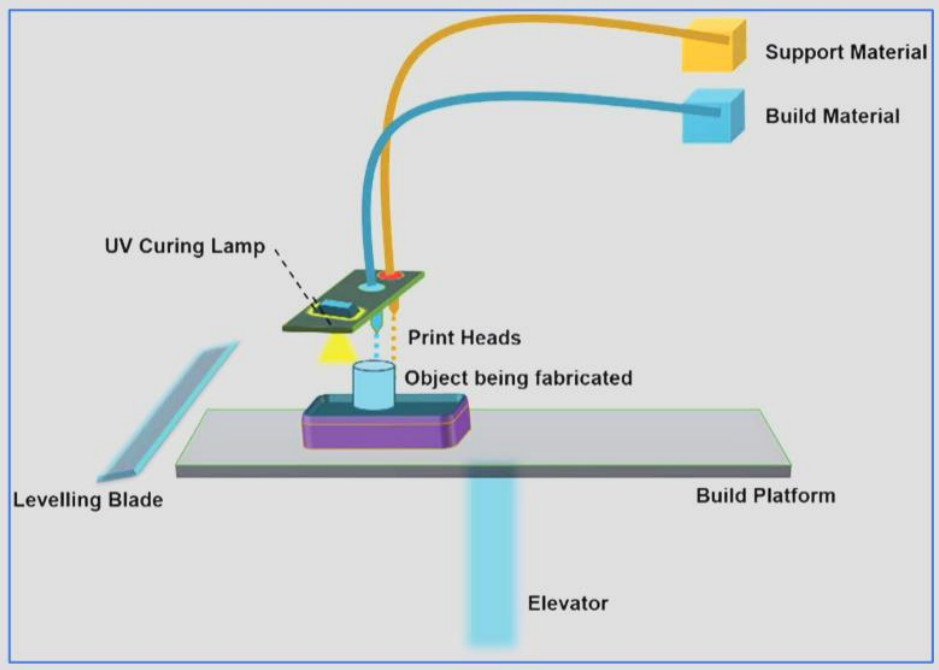

Figure 2.3. Material jetting process (Source: Gülcan et al. 2021)

2.1.2.1 Inkjet Printing

Using ink droplets, inkjet printing is a non-contact digital printing method that transfers digital data from a computer that represents a character or image onto a substrate. Apart from its well-recognized use in document processing as an automated office tool, inkjet technology has also been extensively utilized in the electronics and micro-engineering sectors for printing electronic components (Boland et al. 2006). Figure 2.4

demonstrates a schematic of additive manufacturing of ceramics components by inkjet printing.

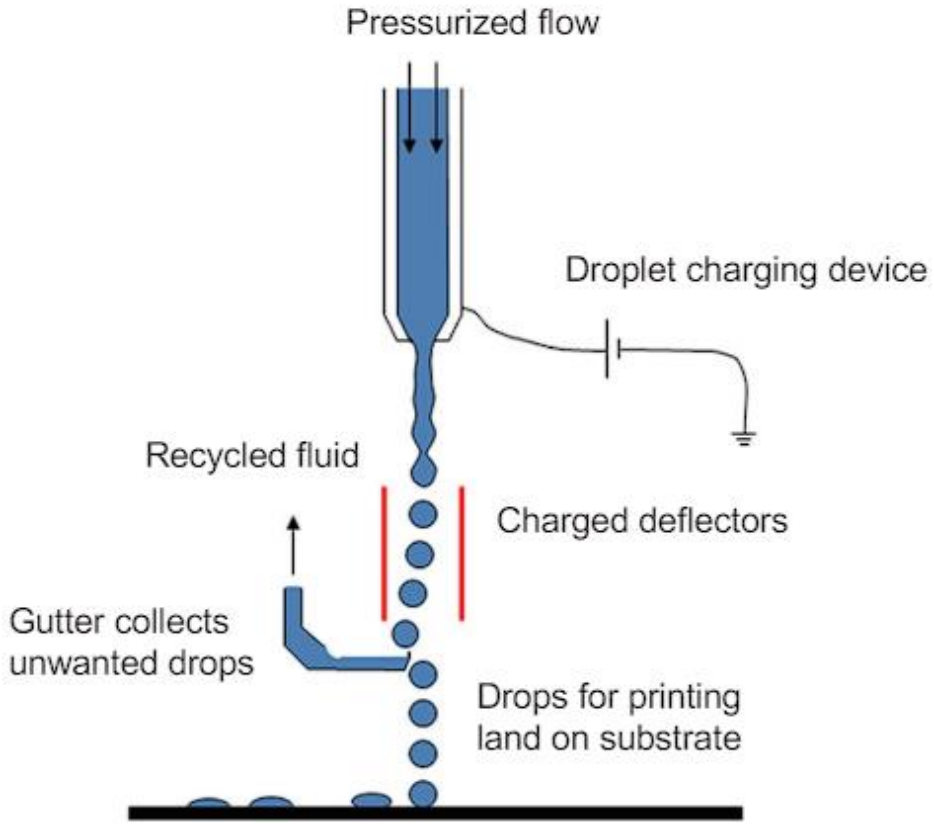

Figure 2.4. Schematic of inkjet printing for ceramics (Source: Derby 2015)

2.1.2.2 Multijet Modeling

The layering concept, which supports most other rapid prototyping methods, is the basis of multijet modeling (MJM) and a simple schematic of the process can be found in Figure 2.5. The MJM uses a three-dimensional inkjet printing-like method to construct its models. Building a single layer of the model, the MJM head travels in the x-y plane, depositing unique thermo-polymer substance only where needed. Every time a pass is made, a UV lamp flashes to cure the thermo-polymer deposit. The platform is moved away from the head (z-axis) once the layer is finished, and the head then starts constructing the subsequent layer (Bikas, Stavropoulos, and Chryssolouris 2016).

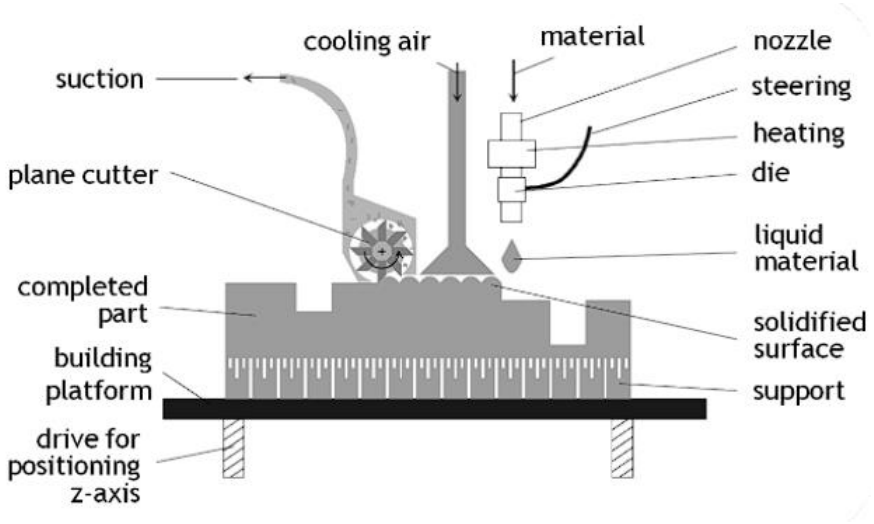

Figure 2.5. Multijet Modeling (Source: Baier and Witt 2014)

2.1.3. Electron Beam Based Processes

This AM technique is called selective electron beam melting, or EBM. In this procedure, the metal powder layer is selectively melted and fused in a vacuum setting using an electron beam. Within a powder bed, a 3D target shape is built layer by layer in accordance with CAD data. EBM provides novel material fusing and melting techniques because of its extremely high velocity limit, inertia-free movement and focus characteristics, and the rapid movement capacity of the electron beam (Uçak, Çiçek, and Aslantas 2022).

2.1.4. Laser Based Processes

Laser-based processes in additive manufacturing refer to a group of fabrication techniques that use laser energy as a primary source to melt and fuse material powder or wire feedstock, layer by layer, to build three-dimensional objects. These processes are characterized by their use of a high-intensity laser beam to selectively melt and solidify regions of a material bed based on digital 3D model data. The most common laser-based AM processes include laser powder bed fusion, laser directed energy deposition (DED) and stereolithography.

2.1.4.1 Stereolithography

The process of local photopolymerization, which is initiated by UV light and occurs in a bath including liquid monomers, oligomers, and photo-initiators, is what makes SLA possible. An increasing number of materials have been developed for a wide range of applications, such as soft robotic actuators, sensors, medical implants, microfluidics devices, and energy storage components, because stereolithography is versatile enough to generate a variety of highly complex 3D structures with high precision and at an affordable cost (J. Huang, Qin, and Wang 2020). A typical stereolithography system can be found in Figure 2.6.

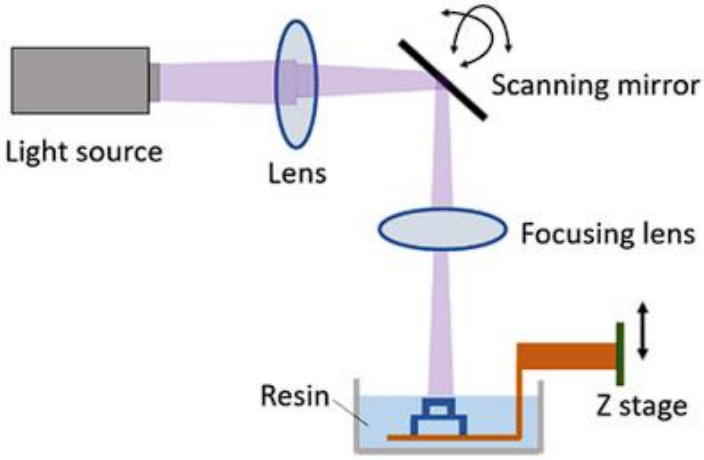

Figure 2.6. A typical stereolithography system (Source: J. Huang et al. 2020)

2.1.4.2 Selective Laser Sintering

Selective laser sintering fuses tiny raw material particles together with a powerful laser to create 3D solid objects. Before printing, in order to reduce thermal distortions, the powder bed is heated slightly below the melting point of the material. The material is locally and partially melted by the energy from the absorbed laser beam, generating the layer contour of the part, while the unsintered powder stays in situ to maintain the structure. Material solidifies as a result of heat transfer via radiation, convection, and conduction as the laser beam travels. Following the layer's solidification, the powder bed is lowered by one layer thickness, and the sintering/build process is restarted with fresh

powder material poured into the newly formed empty space on top of the powder bed. Diverse materials, including metals, polymers, ceramics, and composite materials, can be employed in SLS, along with distinct binding and sintering methods (Papazoglou et al. 2022).

2.1.4.3 Selective Laser Melting

A technique that is comparable to SLS is selective laser melting; the two are variations on the same theme but have different technological aspects, as demonstrated in Figure 2.7. In the selective laser melting method, a part is formed via powder melting as opposed to sintering. As a result, laser beam power is often greater (around 400 W) (Bikas, Stavropoulos, and Chryssolouris 2016)

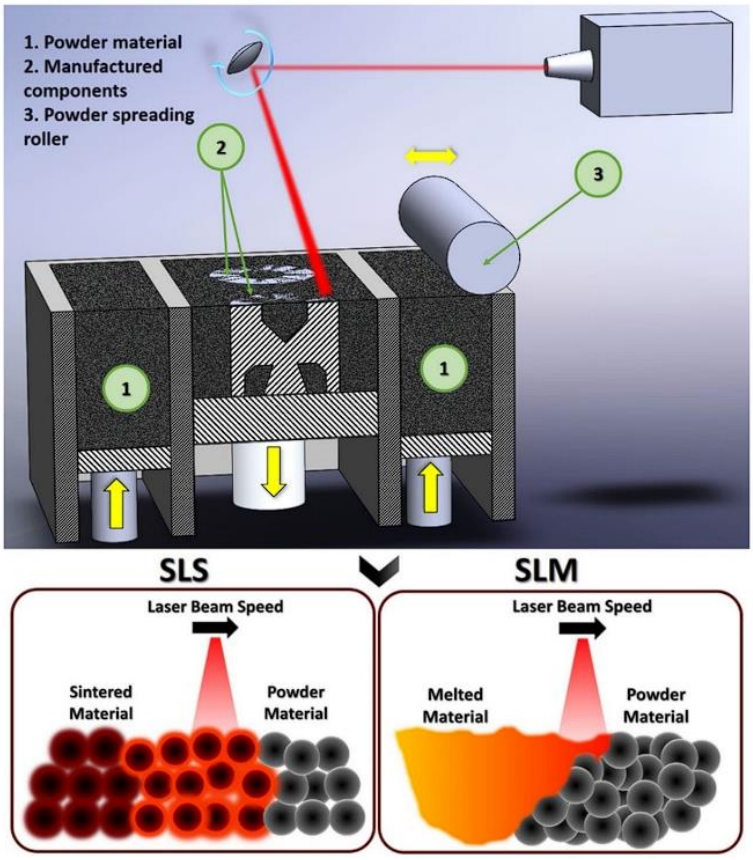

Figure 2.7. Schematic presentation of SLS and SLM processes
(Source: Papazoglou et al. 2022)

2.2. Metal Additive Manufacturing

In recent years, there is a noticeable trend toward AM of load bearing, structural structures, by utilizing the inherent design freedom of such a technique. Since metal is required to construct those structures, industrial applications such as SLM/SLS, and EBM are the focus (Bikas, Stavropoulos, and Chryssolouris 2016).

2.2.1. Directed Energy Deposition

The ISO/ASTM 52900 standard defines the DED process as an additive manufacturing process in which focused thermal energy is used to fuse materials by melting as they are being deposited. Cladding and welding procedures are technologies that are utilized in the DED process. The printed layer is the receiver of thermal energy, such as a laser, electron beam, etc. The feedstock containing various wire and powder types is fed to the thermal energy focused zone simultaneously. Melting of the feedstock and the preceding layer in and around the concentrated thermal energy location creates the molten pool. The molten pool cools to produce the deposit bead. By repeating the aforementioned process, a 3-D metallic component is created (Ahn 2021).

Figure 2.8 showcases two different stock feeding methodologies of powder-fed DED.

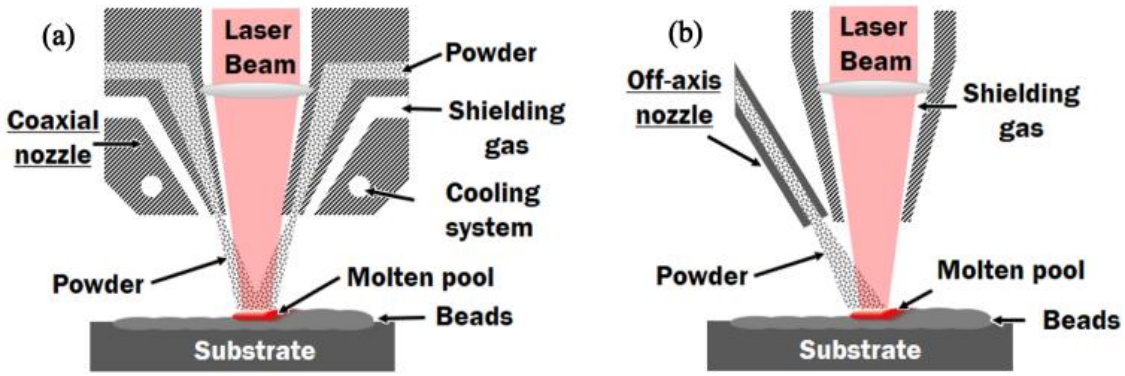

Figure 2.8. Powder feeding methodologies of DED processes: (a) co-axial feeding and (b) off-axis feeding (Source: Ahn 2021)

2.2.2. Laser Powder Bed Fusion

A common metal additive manufacturing technique for producing metallic parts for several industries, including aerospace and biomedical, is laser powder bed fusion. The evenly distributed powder coating is selectively melted using a high-energy laser. Lowering the build table causes the melted area to solidify and distributes a new layer of powder. This procedure is repeated until the part is produced to completion (Kizhakkinan et al. 2023). This process is a sub-branch of SLM and contains several distinct manufacturing parameters such as laser power and scan speed, further discussed in this study and demonstrated in Figure 2.9.

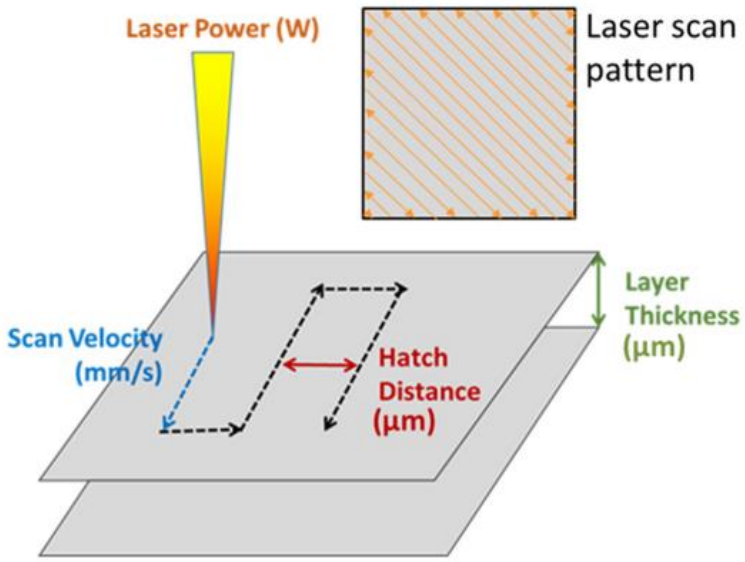

Figure 2.9. Common process parameters in laser powder bed fusion AM (Source: Depboylu et al. 2023)

2.2.2.1 Process Parameters

In L-PBF, the parameters which have the greatest impact are laser power, scan speed, layer thickness, and scan spacing, which is also referred to as hatch distance (Depboylu et al. 2023). Among these parameters, laser power uses the unit of Watts, scan speed is usually denoted by millimetres per seconds, layer thickness has the unit of micrometres and scan spacing millimetres. A schematic of these process parameters, along with process mechanisms and defects can be found in Figure 2.10.

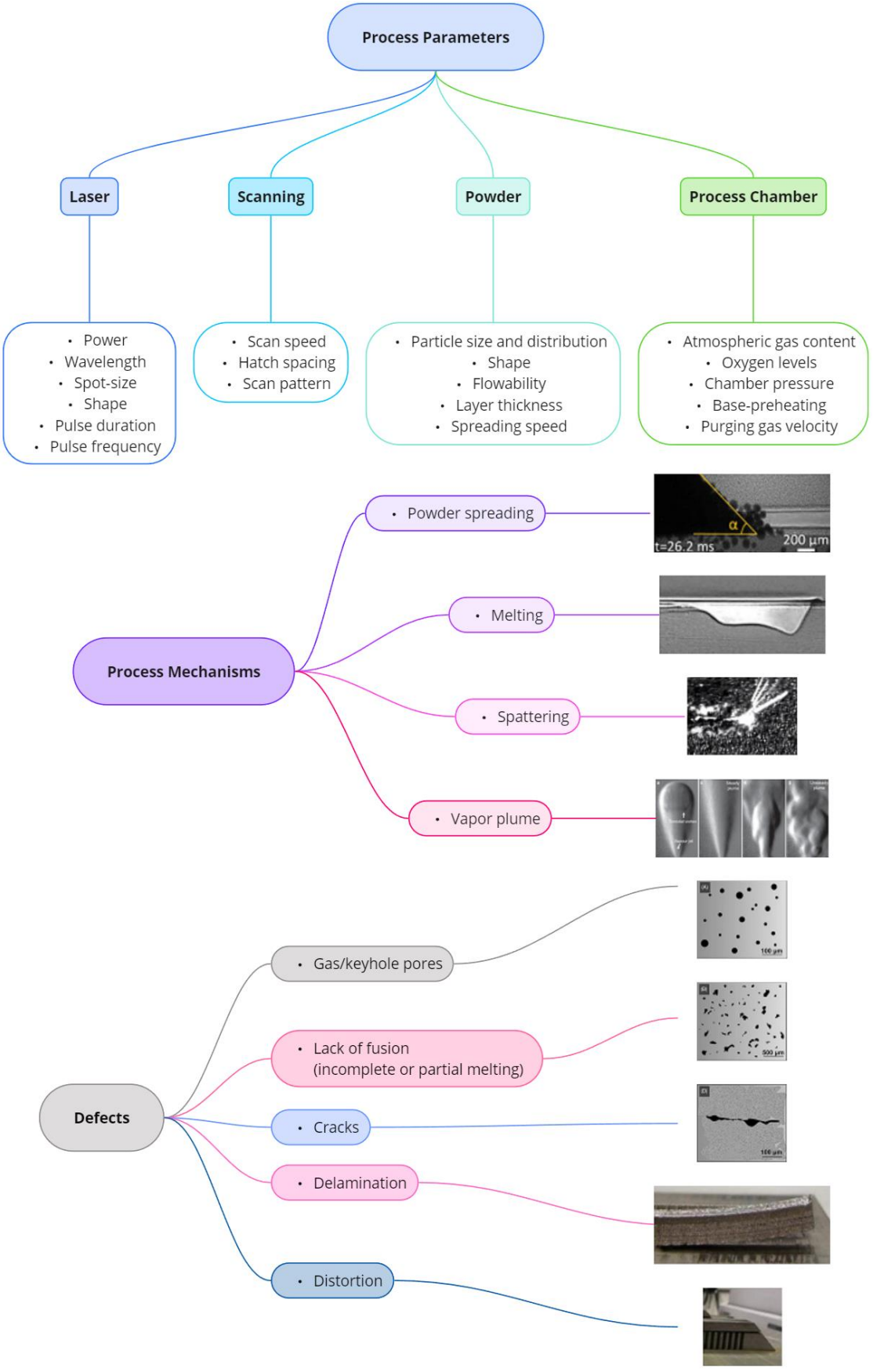

Figure 2.10. Process parameters

2.2.2.1.1 Laser Power

Laser power is measured in Watts and indicates the amount of energy per unit time that is delivered by the laser.

The laser power used in the L-PBF process significantly affects the microstructure and mechanical properties of the resulting products. Studies show that using high-powered L-PBF can produce parts with better tensile properties than die-cast AlSi10Mg (Liu, Wei, and Zeng 2022). It has also been noted that varying the laser power and layer thickness directly affects the cooling speeds, which in turn affects the microstructure and possible performance of the additively built component (Kosiba et al. 2023). Laser power can affect imperfection characteristics in addition to material attributes. When optimum process settings are used, increased laser power can cause hot fractures but also allow for higher build rates, producing extremely dense samples (G. Huang et al. 2022).

Overall, the L-PBF method allows for the efficient manufacturing of high-performance parts with desired material characteristics by altering laser power to modify microstructural features and mechanical qualities to satisfy specific requirements.

2.2.2.1.2 Scan Speed

Another important factor in the laser powder bed fusion process that affects the mechanical, microstructural, and quality characteristics of printed parts is scan speed. Literature review shows a relationship between melt pool shape and crack formation, demonstrating that scan speed, preheating temperature, and laser power may all be tuned to minimize hot cracking while processing high-speed steel HS2-2-2 components (Lücke et al. 2023). According to a different study, different inclination angles and scan speeds have a considerable impact on the surface roughness and near-surface porosity of unsupported overhangs produced by high-speed L-PBF, which can lead to changes in the quality of the final product (Shange et al. 2022). Furthermore, research has demonstrated that scan speed has a significant effect on the texture, grain size, and cell size of stainless-steel components, which in turn affects mechanical characteristics like ductility and tensile strength (Pauzon et al. 2020).

In summary, careful control over scan speed is necessary to maintain ideal component quality in L-PBF and regulate laser-material interactions. It serves as an

example of how differences in scan speed shape the final features of 3D printed components, influencing everything from surface polish to microstructure and from defect generation to mechanical performance.

2.2.2.1.3 Hatch Distance

Hatch distance, or the distance between consecutive scan tracks in L-PBF, is an important factor that affects the final part's mechanical characteristics, surface quality, microstructure, and densification.

A study performed on an AlMgScZr alloy produced by L-PBF revealed that utilizing a hatch distance of 60 μm resulted in nearly complete relative density. Smoother surfaces exhibiting fewer capillary instability were obtained by processing specimens with a hatch distance of 120 μm; no noticeable impact on microhardness was observed. This suggests that surface roughness, microstructural characteristics, and relative density can all be efficiently controlled by hatch distance optimization (Li et al. 2023). The impact of hatch distance on the mechanical anisotropy and microstructure of 316L stainless steel produced by L-PBF was also investigated, demonstrating that changing the hatch distance can change the physical properties of components and enhance printing quality (Z. Zhang et al. 2023).

Overall, hatch distance optimization plays a major role in densification, surface finish, and mechanical performance, making it essential to producing high-quality components in L-PBF. As seen by its critical position in the process parameter combination, the appropriate hatch distance can help reduce common L-PBF concerns like porosity and surface irregularity.

2.2.2.1.4 Deposition Thickness

In laser powder bed fusion, deposition, or layer thickness refers to the thickness of each layer of powder that is melted by the laser during deposition. The productivity, surface quality, and mechanical characteristics of the produced parts are all directly impacted by this parameter.

For the AlSi10Mg alloy, the effect of layer thickness on defect generation and mechanical properties was examined in a study. The results indicated that thinner layers

had better tensile qualities than thicker ones (Liu, Wei, and Zeng 2022). Additional investigation on how layer thickness affects the mechanical characteristics of parts created with L-PBF revealed that greater build speed—which is usually made possible by thicker layers—had an impact on the parts' microstructure and fatigue strength. The results showed a relationship between the layer thickness used and microstructural alterations, increased porosity, and decreased fatigue life (Rautio et al. 2023).

In general, thicker layers present a number of obstacles, including greater defect formation, particularly in the case of porosity, and probably lower mechanical qualities, even though they can greatly increase the building rate and thereby contribute to higher productivity. Careful layer thickness control is necessary to maximize L-PBF's potential for improving production efficiency while maintaining or enhancing material qualities, finding a balance between productivity and component quality.

2.2.2.2 Maraging Steel in Laser Powder Bed Fusion

A kind of ultra-high strength steel called maraging steel is renowned for its remarkable ability to maintain malleability while maintaining a high tensile strength and toughness.

Because of its great strength and ability to gain even more strength by post-process aging, maraging steel is especially well-suited for applications involving additive manufacturing. The final qualities of the printed part are significantly influenced by the manufacturing parameters (Paul et al. 2022). A common option for AM, maraging steel's great strength and simple post-processing make it perfect for obtaining intricate part geometries and high precision (Rao and Rao 2022).

Maraging steel is unique in that it can be produced using additive manufacturing methods such as L-PBF and DED, and it can meet the engineering requirements of high strength, toughness, and ductility. Its applicability across a range of sectors continues to be enhanced by advancements in alloy formation and process optimization. However, maraging steel also comes with its unique hardships.

The mechanical characteristics and manufacturability of tool steels such as maraging steel, as determined by SLM have not been thoroughly studied. Each powder layer goes through multiple phase transitions quickly, and these changes establish the final microstructure and the corresponding mechanical qualities that will come from the

process (Mugwagwa and Dimitrov 2019). Thermal stresses are created during SLM due to the rapid transition from solid to liquid and back again. A brittle martensitic phase is also formed as a result of the quick cooling. Rapid heating and cooling cycles are produced by the localized melting and heating of powders at these high temperatures, as well as by the brief interaction between the powder bed and the high-energy laser beam. This causes thermal stresses to develop in the part that is being solidified. When all of the heat has finally been removed from the material, residual stresses will still be present if these stresses are greater than the yield strength of the material. Part distortion from these stresses manifests as warping or bending, pores, cracks, delamination, and plastic deformation during the consolidation process (Mugwagwa and Lameck 2016).

CHAPTER 3

OPTIMIZATION IN ADDITIVE MANUFACTURING

Many process parameters that affect the printed part are involved in metal AM procedures. The mechanical qualities of the AM component, such as tensile strength, ductility, surface roughness, fatigue life, and hardness, are influenced by the microstructure of the part, which is influenced by the temperature history of the AM process. Producing high-quality AM parts thus requires a thorough grasp and ideal management of the process parameters. It is therefore necessary to identify the ideal process parameters for any given design aim, production objective, and feedstock material. The process parameter optimization of various metal AM materials has been extensively studied in the literature, and AM has been the subject of multiple review studies. The necessity of process parameter optimization in AM is acknowledged and emphasized in the literature (Chia et al. 2022).

In L-PBF, the parameters which have the greatest impact are laser power, scan speed, layer thickness, and scan spacing, which is also referred to as hatch distance (Depboylu et al. 2023). Direct comparisons based solely on combinations of these criteria may be deceptive because the parameters do not exactly correlate in a linear sense. In reality, several parameter combinations with comparable values may result in various mechanical qualities (Chia et al. 2022). Thus, use of optimization methods is required to establish a deeper understanding of these parameters, how sensitively they affect the part and how can they be combined.

3.1. Optimization Stages in Additive Manufacturing

It is possible to methodically condense optimization frameworks in AM into four primary sections: design of experiments, modeling, characterisation (gathering data), and optimization (Chia et al. 2022). Additional steps such as creating external surrogate models or conducting simulations with the data could also be beneficial for optimization of AM. The relationship between these sections is demonstrated in Figure 3.1.

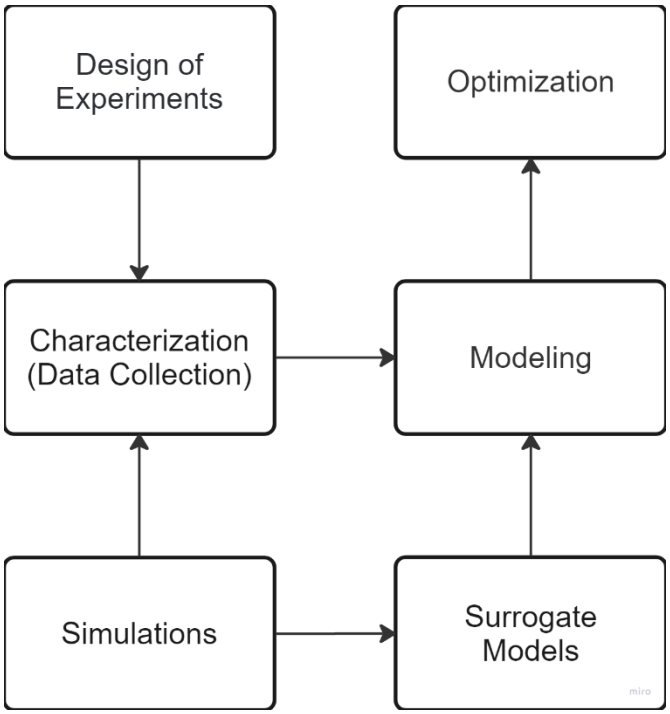

Figure 3.1. Optimization framework in AM summarized into four sections: design of experiments; characterization; modeling; optimization (Source: Chia et al. 2022)

3.1.1. Design of Experiments

The application of Design of Experiments (DoE) in decision-making has spread to numerous industries, whether in the context of manufacturing process optimization, new product creation, or both. It is employed not just in the engineering field but also in the fields of administration, marketing, healthcare, pharmaceuticals, food, energy, and architecture. DoE is relevant to both computer simulation models and real-world systems (Durakovic 2017).

DoE is a multivariate experimental design in which two or more variables (sometimes referred to as factors) are consistently examined in a single experiment. It is the most effective way to conduct experiments when defining variable effects is crucial to achieving a goal. Even with DoE, the more study variables there are, the more work there is (Porter, Verseput, and Cunningham 1997).

Even though it can require a large number of experiments, DoE enables the identification of optimal conditions for achieving desired performance outcomes. Predictive models can be developed more easily when important interactions and

significant outcomes are found in the analysis of experimental data. By identifying the set of parameters that produce the greatest outcomes, these models guide the optimization process. In the end, DoE optimization results in increased product quality, decreased costs, and better process performance, making it a crucial tool for industrial and technical applications.

DoE has been used in previous works mentioned in this study, where several different combinations of AM parameters are utilized in a design of experiment fashion to get varying deformation results (L. Mugwagwa et al. 2018).

3.1.2. Modeling

Modeling stage creates a link between the input and output parameters of the optimization problem and acts as the processing unit where the input data is shaped into a comprehensive form where the shape of the input would allow outputs to be coherently processed. Inspecting Figure 3.2 from top to bottom demonstrates a sample modelling problem where physical or numerical experiments are conducted to gather data, and then the data is used incorporated into a suitable modeling technique.

In metal AM, certain forms of modelling like Kriging and neural networks have been utilized (Chia et al. 2022).

Parameter sensitivity studies could also be conducted during the modeling stage as sensitivity analyses tend to be integral to the model development. Such studies can give results about how inputs correlate with eachother and what types of outputs are affected in what scale.

For this study, the modelling stage uses finite element analysis for the direct optimization and tabular data along with metamodel prognosis for the stochastic optimization.

3.1.3. Characterization

The data acquisition, or characterization, in this study can be split into two parts. First part is the data acquired from literature (L. Mugwagwa et al. 2018) where a benchmark part has been printed with ranges of parameters in order to calculate the influence of process parameters, hence consisting of a design of experiment method. The

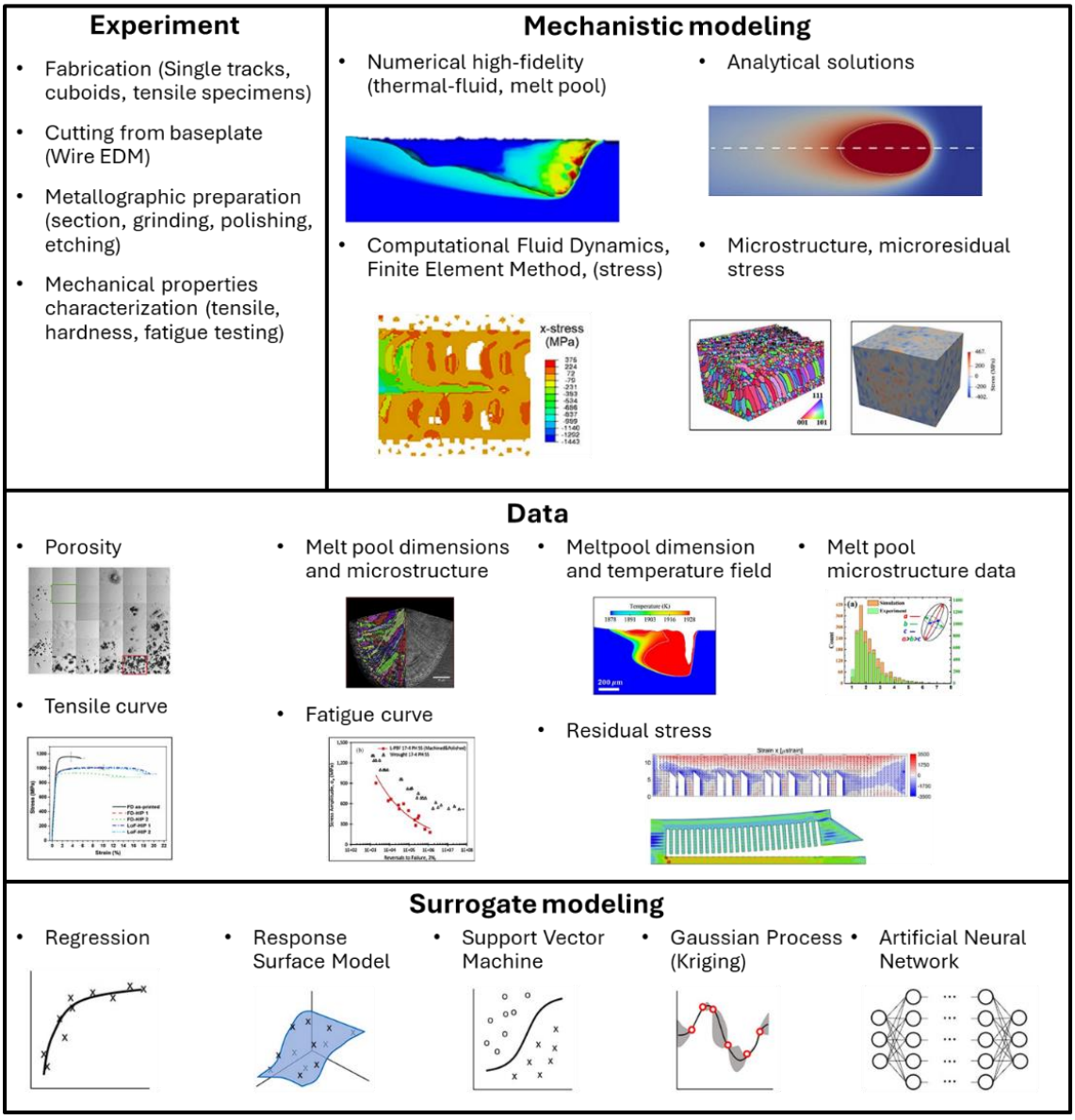

Figure 3.2. Modeling for optimization in AM (Source: Chia et al. 2022)

second part is where the simulation model of the same part is calibrated so that simulations yield the same results as the physical parts. The first stage has been conducted via a DoE method (L. Mugwagwa et al. 2018) while the second stage follows a single objective direct optimization method. Data for the first stage is given in Table 3.1, while the data for the second stage, with further explanation, is discussed in Chapter IV.

The data presented in Table 3.1 originates from literature (L. Mugwagwa et al. 2018) and focuses on measuring the displacement at the tip of the printed part after the majority of the part has been cut off from the baseplate. Therefore, the maximum deflection column of Table 3.1 is the measured maximum distortion.

3.1.4. Optimization

Every optimization study starts with the definition of an optimization problem. The method, inputs, outputs, and objectives vary but the problem at hand should be stated. In order to obtain the problem, the study must be thoroughly investigated. For a problem to exist, an objective is created which can either be to minimize the work necessary or maximize the intended benefit. Problem definition is the process of figuring out the conditions that yield the maximum or least value of a function since the amount of work needed or the expected benefit in any real-world scenario can be described as a function of specific decision variables. Given a set of restrictions, optimization techniques can be used to find the minimum of a function involving multiple variables.

Table 3.1. Design of experiment data of L-PBF samples (Source: Mugwagwa et al. 2018)

Inputs			**Outputs**		
Layer thickness (μm)	Laser power (W)	Scanning speed (mm/s)	Relative density (%)	Porosity (%)	Maximum deflection (mm)
30	80	400	88.48	11.52	0.5
30	80	300	90.98	9.02	0.39
30	80	200	94.75	5.25	0.18
30	100	500	96.04	3.96	0.74
30	100	400	95.97	4.03	0.51

Cont. on next page

Table 3.1. (cont.)

30	100	300	91.03	8.97	0.33
30	120	500	98.04	1.96	0.87
30	120	400	95.63	3.47	0.65
30	120	300	93.89	6.11	0.34
30	140	600	98.77	1.23	0.89
30	140	500	96.9	3.1	0.88
30	140	400	96.27	3.73	0.71
30	160	700	99.06	0.94	1.1
30	180	700	99.35	0.65	1.16
30	160	600	98.91	1.09	1.03
30	160	400	96.59	3.41	0.81
30	160	300	95.39	4.61	0.65
30	160	800	96.35	3.65	1.13
30	180	800	99.21	0.79	1.16
30	180	900	97.77	1.23	1.09
30	180	1000	98.47	1.53	1.18
30	180	600	99.58	0.42	1.04
30	180	500	98.62	1.38	0.87
30	180	400	94.89	5.11	0.38
45	120	400	90.42	9.58	0.2
45	120	300	90.06	9.94	0.14
45	120	200	89.76	10.24	0.25
45	120	500	95.81	4.19	0.41
45	140	400	90.59	9.41	0.13
45	140	300	91.62	8.38	0.02
45	160	500	95.86	4.14	0.12
45	160	400	95.24	4.76	0.1
45	160	300	92	8	0.01
45	180	600	99.35	0.65	0.51
45	180	500	98.48	1.52	0.3
45	180	400	89.72	10.28	0.09
45	180	300	92.91	7.09	0.07

Stochastic search techniques can be applied to evaluate issues described by a set of random variables with known probability distributions. To obtain the most accurate representation of the physical condition, statistical approaches allow the analysis of experimental data and the creation of empirical models (Rao 2019).

An optimization or mathematical programming issue is defined as follows:

$$\text{Find } X = \begin{Bmatrix} x_1 \\ x_2 \\ . \\ . \\ x_n \end{Bmatrix} \text{ which minimizes f(x)} \tag{3.1}$$

depending on the conditions

$$g_j\,(X) \leq 0 \quad j = 1,2,\ldots,m \tag{3.2}$$

$$l_k\,(X) = 0 \quad k = 1,2\ldots.,p \tag{3.3}$$

Here, $f(X)$ is the objective function, $g_j(X)$ and $l_k(X)$, respectively, are the inequality and equality constraints, and X is an n-dimensional vector known as the design vector. The number of constraints m and/or p and the number of variables n do not have to be related in any manner. The optimization problem in Equation 3.1 is referred to as a constrained optimization problem. There are certain optimization problems that are unconstrained, or that have no limitations (Rao 2019).

Since this study utilizes two different optimization methods, two different optimization problems have been defined. For the first optimization problem, where DoE data is given to the simulation model and direct optimization is utilized in order to match the data from experiments, the problem definition was to “seek targets”. The target being sought was the deformation results from the experimental data. The second optimization problem, where a stochastic algorithm was used, had the problem definition of “minimize results” where the deformation of the printed part, hence residual effect of AM was minimized.

3.1.4.1 Genetic and Evolutionary Algorithms

Algorithms inspired by nature, like the genetic algorithm (GA), are becoming more popular for resolving challenging engineering problems. GA creates a system of mathematical equations to address challenging non-linear issues. Initially presented by (J R Koza 1992), GA uses machine-learning methods to use Darwinian natural selection to symbolically optimize a set of mathematical solutions. In order to mimic the biological evolution of survival of the fittest, the GA technique employs three main processes: crossover, mutation using a population of feasible solutions, and selection or reproduction. A regression method assumes a basic type of relationship between independent and dependent variables. Next, the parameters of the model are selected to maximize its fit to the data. This is a disadvantage of conventional regression techniques, which base their analysis on a predetermined polynomial function (Altıntaş and Artem 2021).

The method by which variation is incorporated into the population distinguishes the two primary forms, evolution algorithms (EA) and genetic algorithms (GA). The majority of variety in genetic algorithms arises from gene recombination through crossover operators, although adaptive mutation for evolution techniques adds variation to the population, as can be seen in Figure 3.3.

Efficiency values must be assigned in order to choose individuals for reproduction using random selection techniques. The scalability issue with the proportional fitness assignment is resolved by using a rank-based fitness assignment. The likelihood of choosing a design with poor fitness is low because of the random selection process and the fitness ranking. But since it's not impossible, a weak design might likewise be used to the generation of newer iterations.

By sharing information between chromosomes, two parent individuals can produce two children through a recombination mechanism called the crossover operator. The goals are to preserve population diversity (exploration) and acquire individuals who have superior qualities (exploitation).

In genetic algorithms, crossover is considered to be the primary search operator (ANSYS 2024).

Evolutionary algorithms on the other hand are a branch of artificial intelligence that solves optimization issues by simulating natural evolution. The survival

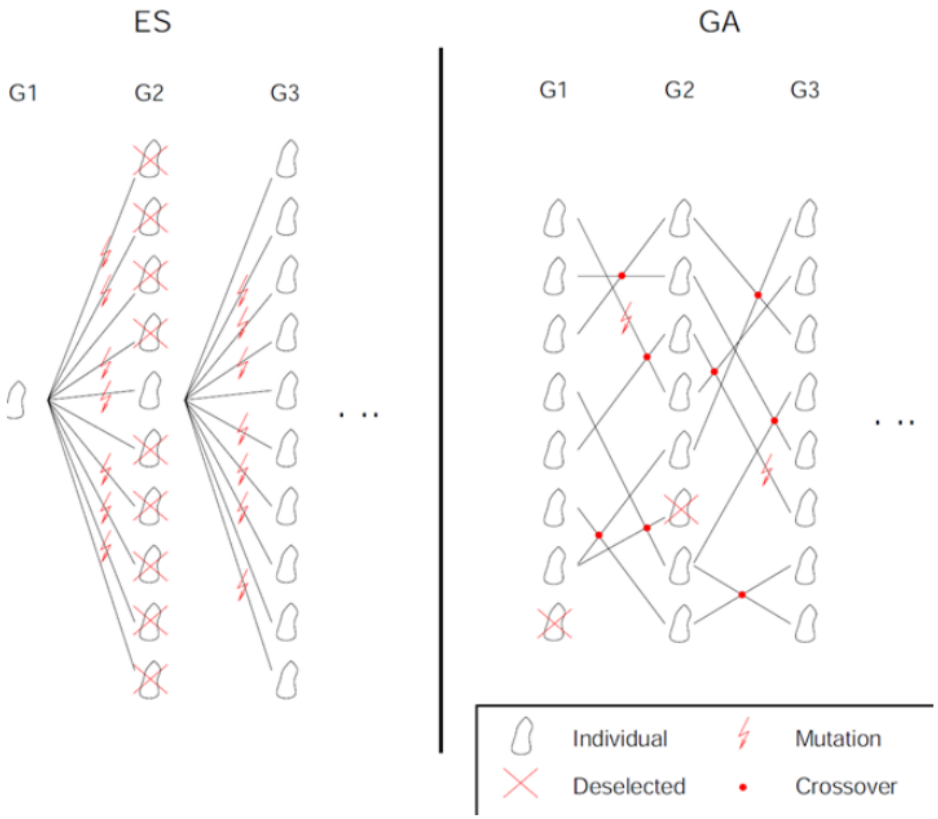

Figure 3.3. Evolutionary and genetic algorithm working structures
(Source: ANSYS 2024)

of the fittest theory, which holds that the best or most optimal solutions to a problem emerge over generations, is the foundation upon which EAs function. Selection, mutation, recombination, and inheritance are the main mechanisms of evolutionary algorithms. By utilizing and exploring the search space, these mechanisms direct the evolutionary process towards optimal solutions.

Finding several minimum components in a single iteration inside partially sorted combination sets is one of the unique characteristics of evolutionary algorithms. EAs are very useful in tackling difficult optimization problems where traditional approaches may fail because of this feature, which is especially prized for its efficiency in getting to the set of minimal elements within a finite number of iterations (Rudolph 1999).

At the beginning of an evolutionary algorithm, μ number of parents of the starting population of P_t produce λ offspring in some probabilistic functionality ($\lambda \geq \mu \geq 1$). Members of the new generation, or the offspring, are harvested in a set of Q where identical offsprings might exist and are not removed from the population pool. Those among Q yielding optimal values for the objective are moved to Q^*. As the creation of

the first offspring generation comes to an end, the new generation is partitioned into the sets of Q and Q^* where $|Q^*| \geq 1$ and $|Q| + |Q^*| = \lambda$. Each member of Q is expected to demonstrate lower qualities than offsprings is Q^*.

For the following generation, for each offspring q from Q^*, given that the parent pool P_t only contains the first offspring generation, all parents from P_t that yield worse results than the members of offspring q are separated and discarded from P_t. Then, the offspring q is moved from Q^* to P'. If no older generations yield worse results than the offspring q, and it is incomparable to none in the parent pool, then q is relocated from Q^* to Q'. As the second generation stops populating, P' has the more successful offsprings that are better than most parents, Q' has offsprings that are either better than some parents or those incomparable to all parents and Q^* has offsprings that are worse than most parents. Older generations that are not partitioned into any newer sets, left in P_t, are incomparable to each offspring in $P' \cup Q'$. Entire set of Q is expected to have lower qualities than any member of $P' \cup Q' \cup Q^*$.

After the second generation, the pool P_{t+1} parents of the third and following generations consist of the members of P' and any residual left in P_t. At that stage, for the members of P_{t+1}, $|P_{t+1}| = |P_t \cup P'| = |P_t| + |P'| \leq \mu$ is expected.

If $|P_{t+1}| < \mu$ then members of Q' are relocated to P_{t+1}. If Q' contains more than expected members to increase the population of P_{t+1}, artificial set of rules may be applied to filter which members of Q' are selected to populate P_{t+1}. If Q' contains less than expected members to increase the population of P_{t+1}, artificial set of rules may be applied to filter which members of Q^* are selected to populate P_{t+1}, and at some cases, similar procedures may be applied to Q aswell. Given that $\lambda > \mu$, each new following population can continue with a completed population of at least μ members. For the case of any λ having less than its respective μ, P_{t+1} may be filled with randomly created members.

At the end of any following generation, each individual of the original population, P_t, who was not overqualified by some offspring are passed to the newest population, P_{t+1}, while each member of the previous populations that had lower qualities than some offspring are replaced by newer and better generations (Rudolph 1999).

Evolutionary algorithms provide a reliable computational method for solving optimization issues in a variety of domains. Their ability to adapt and find the best answers for intricate, multi-dimensional issues derives from their origins in the theories

of natural selection and evolution, which positions them as a key technology in optimization research.

3.1.4.2 Metamodel of Optimal Prognosis

Metamodel of Optimal Prognosis (MOP) was developed as an automated technique to find the optimal filter meta-model configurations by Dynardo (Will and Most 2009). MOP eliminates the need for additional analysis by enabling the testing of several design configurations using a proxy model of the real physical problem. A metric for describing estimate quality must first be defined before an automation technique can be constructed. This eliminates the need for additional analysis by enabling the testing of several design configurations using a proxy model of the real physical problem. Specifically, the MOP uses the generalized Coefficient of Determination (CoD) to provide pure polynomial regression. To evaluate the accuracy of an approximation in a polynomial regression, the CoD calculates the proportion of variance explained by the approximation:

$$R^2 = \frac{SS_R}{SS_T} = 1 - \frac{SS_E}{SS_T};\ \ 0 \leq R^2 \leq 1 \tag{3.4}$$

In Equation 3.4, when SS_T is used to formulate total variation, SS_R is used to determine variation in regression and SS_E is used to dictate unexplained variance, as can be seen in Equation 3.5:

$$SS_T = \sum_{i=1}^{N}(y_i - \mu_Y)^2, SS_R = \sum_{i=1}^{N}(\hat{y}_i - \mu_{\hat{Y}})^2, SS_E = \sum_{i=1}^{N}(y_i - \hat{y}_i)^2 \tag{3.5}$$

However, to avoid unnecessary fitting, the modified coefficient of determination, given in Equation 3.6, was developed:

$$R^2_{adj} = 1 - \frac{N-1}{N-p}(1 - R^2) \tag{3.6}$$

There are *N* sample points and *p* regression coefficients. The prognostic quality was used to evaluate an approximation's quality using an extra test data set. The degree of agreement between the estimates from the meta-model and the actual test data is measured by the coefficient of prognosis. CoP is specified in Equation 3.7 by (Will and Most, 2009).

$$CoP = \left(\frac{E\left| Y_{test} * \hat{Y}_{test} \right|}{\sigma_{Y_{test}} \sigma_{\hat{Y}_{test}}} \right)^2 ; 0 \leq CoP \leq 1 \tag{3.7}$$

An optimal metamodel can be identified with a defined CoP. Every possible significance is investigated for each meta-model by varying the significance percentage from 99% to a predetermined minimum value. After that, a polynomial regression is constructed, and Equation 3.8 is used to determine the coefficients of significance (CoI) for every variable.

$$CoI_{Y,X_i} = R^2_{Y,X} - R^2_{Y,X\sim i} \tag{3.8}$$

The CoD of the reduced model, which takes out all linear, quadratic, and interaction terms from X_i, is represented by $R^2_{Y,X\sim i}$, whereas the CoD of the complete model, which contains all terms of the variables in *X*, is represented by $R^2_{Y,X}$.

A specified value is used in place to cover the 1% threshold in the CoI_{Y,X_i} calculation. Each variable's CoI is used to build the meta-model and determine the coefficient of prognosis. The optimal meta-model is chosen from the maximal configuration of CoP. The meta-model is constructed using the training data set, and the CoP is computed using the test data set.

Alternatively, a merged data set comprising both test and training data is utilized for significance filter correlations and importance filter regression. To maintain similarity in answer ranges across training and test sets, the original data set is divided into these subsets if an additional test data set is unavailable. This division makes sure that the distribution and characteristics of the entire data is preserved. By utilizing the full spectrum of available data, this approach provides a balanced evaluation of the model's performance.

3.1.4.3 Stochastic Design Improvement

Without requiring in-depth understanding of potential relationships in design space, Stochastic Design Improvement (SDI) is a local, single-objective optimization process that enhances a suggested design through the use of a straightforward stochastic technique. From an initial start design, a uniformly distributed Latin Hypercube Sampling within a defined range produces a start population of size μ. As seen in Figure 3.4, the best design is chosen as the new centre point for the sample of the subsequent iteration at each iteration stage.

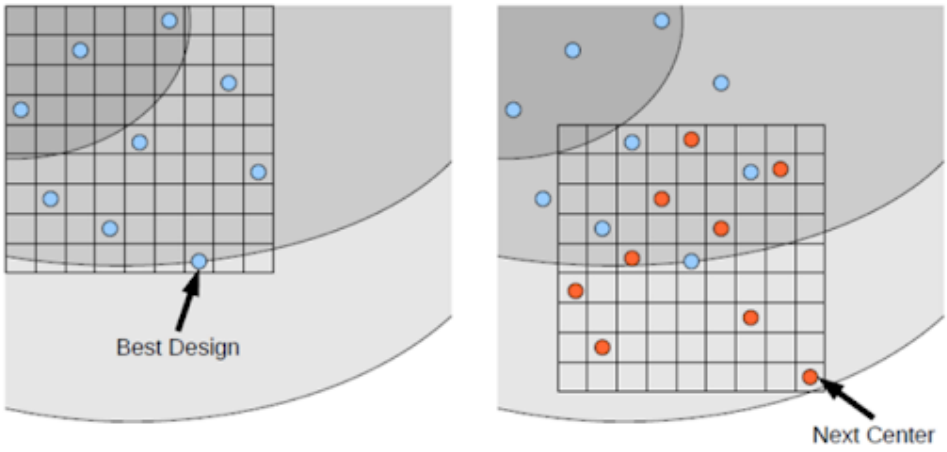

Figure 3.4. Stochastic design improvement (Source: ANSYS 2024)

At every iteration, the sampling scheme's ranges are modified. The population as a whole may relocate to a better area and improve every step, depending on the optimization problem. Using the parameter-free constraint management technique used in evolutionary algorithms, all individuals of a single iteration will be compared with respect to the aim and constraints. The algorithm converges if the maximum number of iterations is reached, if a given improvement over the original design is gained, or if a specific performance decrease is noticed between two iteration steps (ANSYS 2024).

The SDI is particularly robust and works for a large number of unsuccessful designs, discrete and continuous parameters, design variables, and constraint conditions because of its pure stochastic approach. It was not intended to uncover globally ideal solutions, but rather to enhance a preliminary design. Because of this, its efficiency might be much lower than that of evolutionary algorithms (ANSYS 2024).

CHAPTER 4

SIMULATION IN ADDITIVE MANUFACTURING

Simulation of the metal additive manufacturing laser powder bed fusion process requires realistic adaptation of manufacturing and real-world parameters into numerical modeling. This chapter investigates the methodologies used in this thesis.

4.1. Finite Element Analysis

A popular computer tool in engineering, finite element analysis enables the analysis of complicated structures under varied loading scenarios and boundary conditions. Fundamental to mechanical engineering, finite element analysis breaks down large, complex problems into smaller, more computationally manageable parts. In order to better understand the likelihood of failure or other problems, engineers can use this approach to forecast how materials and structures will behave under stress, strain, or temperature influences.

FEA is essential for enabling structural study of creating irregular geometry, by means of semi-automated processes that translate three-dimensional point clouds into finite element models. This tackles the problem of preserving and restoring complex geometry, where conventional CAD-based models might not be adequate (Castellazzi et al. 2015). Differential equations that explain physical processes are solved at the core of FEA. The behaviour of the material or structure under investigation is generally represented by a set of equations that define each finite element. These components come together to form a mesh because they are joined at what are referred to as nodes. An isolated representation of the geometry under study is provided by the mesh. Predicting the values of the physical quantities throughout the domain requires FEA software to build the equations at each node and solve them concurrently.

First step of FEA is pre-processing. During this stage, the problem's physical boundaries, including its geometry, material qualities, boundary conditions, and loading circumstances, must be defined. This stage, in which the domain is discretized into finite elements, depends critically on mesh generation (Bathe 1996).

Next step is solution, where, based on the inputs, FEA software calculates the behaviours in each element and node. Numerical approximations for stresses, strains, or other desirable physical parameters throughout the whole problem domain are obtained by solving the mathematical models.

In the last stage, the simulation's outcomes are visualized, examined, and interpreted. Engineers, depending on the nature of the problem, can look at temperature fields, fluid velocities, or detailed distributions of stresses and deformations (Zienkiewicz, Taylor, and Zhu 2005).

Since FEA consists of model discretization, a load can be applied to entire geometries or to local features. Results, just like loads, can be interpreted for entire models or for local features. Both linear and nonlinear analyses—the latter of which addresses complexities including geometric nonlinearities, material nonlinearities, and contact mechanics—might be included in FEA (Kim 2015). Figure 4.1 investigates a linear finite element analysis, where the change in input is expected to behave in a linear fashion accordingly to the output. While problems solved in FEA can range from simple to extremely complicated, the quality of the input data and the resolution of the mesh have a major impact on the accuracy of the outcomes.

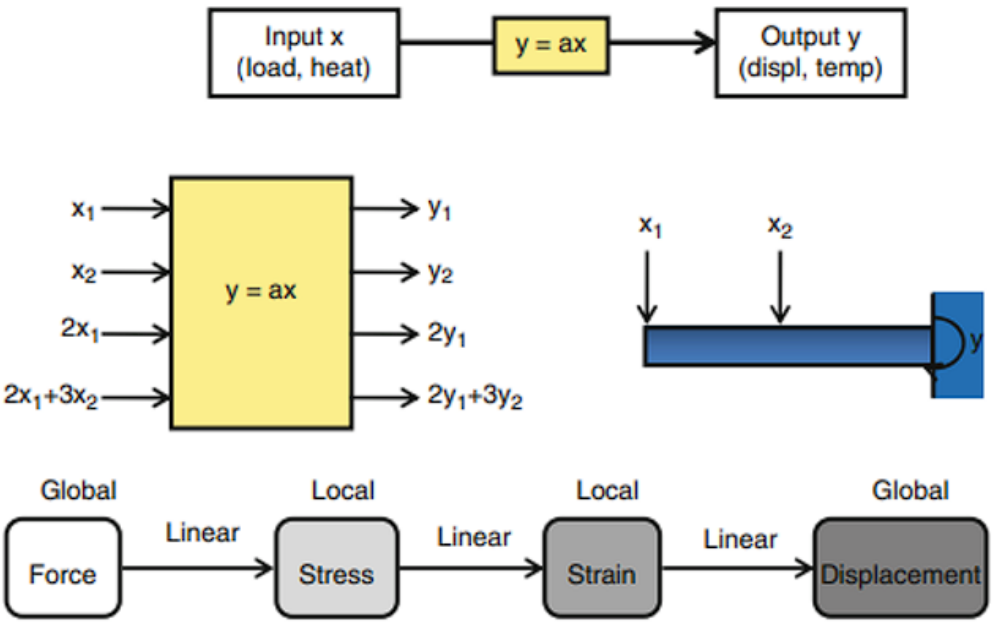

Figure 4.1. Linear relationship of input and output in FEA (Source: Kim 2015)

4.2. Additive Manufacturing Simulation

In additive manufacturing, finite element analysis is essential, particularly when examining the behaviour and performance of lattice structures in interbody cages. The body-centered cubic (BCC) structure is one lattice arrangement that has been found to produce optimal stress and strain values through FEA studies. These results are important for the design and operation of AM components (Bozyiğit et al. 2023).

When using wire arc additive manufacturing (WAAM), FEA is also crucial for examining various scanning patterns and energies that impact residual stress and deformation. These findings have important implications for improving the AM process and the quality of the finished manufactured parts (Ali and Han 2023). In laser-based metal additive manufacturing types, factors including laser power, scanning speed, and strategy are crucial because they affect the location of stress in the cladding layers. Essential factors in the creation of the AM process, FEA aids in finding these parameters to lower stress and enhance part quality (Meng et al. 2023). Residual stress in functionally graded materials produced by laser additive manufacturing has been predicted and managed using finite element analysis. The residual stress of the form can be optimized by varying the laser energy and composition of the transitional layer material, which is a major concern in MAM (Zhao et al. 2022).

While AM includes microscale, mesoscale and macroscale phenomena, FEA of AM is usually only interested in the macroscale formations, ignoring some mesoscale and most microscale settings (ANSYS 2024).

In FEA, simulation of PBF process is mainly divided into two main subjects as inherent strain and thermal-structural methods.

4.2.1. Inherent Strain and Thermomechanical Methods

Inherent strain simulations are structural only calculations where effects of temperature during the printing process are ignored by the solver. Instead of calculating the thermal properties, inherent strain studies utilize a factor named “Strain Scaling Factor” where thermal effects are artificially added instead of solved.

For the Inherent Strain approach, necessary material information are mechanical properties such as Poisson’s ratio, Young’s Modulus, Yield Strength, Bilinear or

Multilinear Hardening Curves that are temperature independent. Temperature dependent properties are not required unless a thermal simulation, such as heat treatment, is going to be solved (ANSYS 2024).

Stress is necessary for the strain to fit inside the body and for the inherent strain technique to work. If we consider this to be a mechanical process, the body must be distorted in order to accommodate the strain field. After removing the loads necessary to cause the body to deform, equilibrium is reached to determine the residual stress state. Phase transformation, thermal strain, plastic deformation, and other processes may result in the poorly fitted strain field. The term "inherent strain" refers to the sum of all such potential sources of incompatible strain that exist within the body. The inherent strain, or strain that does not fit, is what causes any tension to exist in the unloaded body (Hill et al. 1999).

A relationship between the stress change resulting from aforementioned processes is requested for the stress, σ, and the inherent strain field within the body, ε^*, assuming that the material behavior of the body is linear elastic. The following tensor is used for the representation of this relation:

$$\sigma = f(\varepsilon^*) \tag{4.1}$$

Here, $f()$ is a second order tensor function while σ and ε^* are second order tensor functions of the spatial coordinates. Considering the distribution of intrinsic strain, $f()$ denotes a somewhat complicated set of methods needed to solve for stress.

According to the constitutive relation for an elastic material, inherent strain enters the elasticity problem as:

$$\sigma = C \cdot (\varepsilon - \varepsilon^*) \tag{4.2}$$

where C is the elastic constitutive tensor. The total strain must be found to satisfy the equilibrium problem of the application of an inherent strain to any problem (Hill et al. 1999).

Thermomechanical simulations, on the other hand, solve for both structural and thermal loads. These simulations require temperature dependent material properties such as specific heat capacity, temperature dependent Poisson’s ratio etc. Thermomechanical simulations use a weak coupling that constitutes convergence between both the

temperature and structural fields. Weak couplings are also called load vector or sequential couplings. These equations have the stiffness matrix account for the dependency of $[K_{11}]$ and $\{F_1\}$ on $\{X_2\}$ as well as $[K_{22}]$ and $\{F_2\}$ on $\{X_1\}$ in Equation 4.1, whereas $[K_{11}]$ and $[K_{22}]$ are stiffness matrix variables, $\{F_1\}$ and $\{F_2\}$ are force vectors and $\{X_1\}$ and $\{X_2\}$ are two types of degrees of freedom. Instead of having a single degree of freedom, due to the coupling nature of the problem, coming from both structural and thermal solvers, has two different degrees of freedom.

$$\begin{bmatrix} [K_{11}(\{X_1\},\{X_2\})] & [0] \\ [0] & [K_{22}(\{X_1\},\{X_2\})] \end{bmatrix} \begin{Bmatrix} \{X_1\} \\ \{X_2\} \end{Bmatrix} = \begin{Bmatrix} \{F_1(\{X_1\},\{X_2\})\} \\ \{F_2(\{X_1\},\{X_2\})\} \end{Bmatrix} \quad (4.1)$$

In thermomechanical AM simulations, the movement of the laser is not followed as the laser moves very quickly and a whole layer can be created in a very short amount of time. Instead, entire layers are assumed to be manufactured at once. These simulations assume the thermal effects in the printing direction are more dominant than those at in plane direction (ANSYS 2024).

Thermomechanical AM simulations in ANSYS do not constitute the thermal-structural coupling via power equations, but instead follow the temperature changes during the process, as shown in Figure 4.2. This means that while the actual printing process has parameters connected to laser power, simulations will be using the temperature data instead of laser power related parameters.

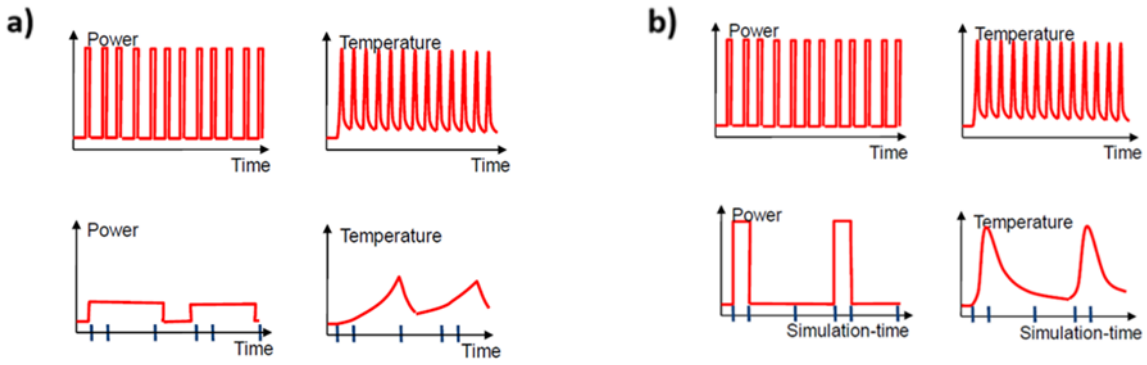

Figure 4.2. Laser power application strategies in FEA of AM where a) demonstrates power application by energy and b) demonstrates power application by temperature (Source: ANSYS 2024)

4.2.1.1 Strain Scaling Factor

Inherent Strain simulations make use of an artificial coefficient named the Strain Scaling Factor. This factor enables the extremely fast and accurate solution of AM simulations without the inclusion of thermal properties. In order to calculate this property, benchmark parts are printed beforehand and measured for several aspects of potential errors.

Manual measurement methods include measuring deformations with a calliper, micrometre or a digital height gage while more automatic measuring methods utilize tools such as Coordinate Measurement Method (CMM) or laser scanners. Dimension differences, or error, between the printed part and the CAD model are then calculated in order to get the strain scaling factors. Strain scaling factors can work in 3 translational dimensions, can optionally include the laser traveling direction or not, depending on the simulation. Equations 4.2, 4.3 and 4.4 demonstrate how the strain scaling factor is factored in when conduction the calculations.

$$\varepsilon_{xx} = SSF * \frac{\sigma_{yield}}{E} \tag{4.2}$$

$$\varepsilon_{yy} = SSF * \frac{\sigma_{yield}}{E} \tag{4.3}$$

$$\varepsilon_{zz} = SSF * \frac{\sigma_{yield}}{E} \tag{4.4}$$

The strategy given in Equations 4.2, 4.3 and 4.4, where *SSF* is the strain scaling factor, σ_{yield} is the yield strength of the material, *E* is the elasticity modulus and ε_{ij} is the calculated strain for the respective direction, will lead to a uniform change of deformation in X, Y and Z directions. This effect is only assumed to happen when the laser scanning strategy follows a chessboard pattern, given in Figure 4.3 (ANSYS 2024).

For the case of other scanning patterns, like the singular direction pattern given in Figure 4.4, more variables are added to the strain scaling factor calculation to include the effects of laser scan pattern, given in Equations 4.5, 4.6 and 4.7. Patterns other than the chessboard pattern require the calculation of these additional variables in order to calculate realistic strains.

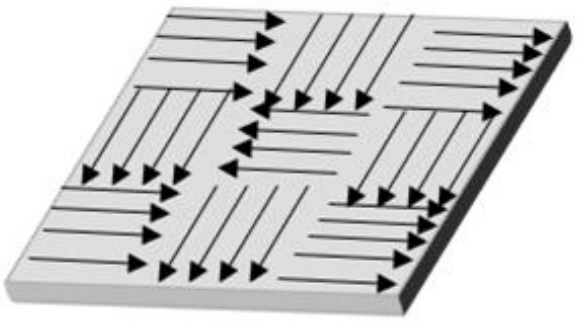

Figure 4.3. Chessboard scanning pattern (Source: ANSYS 2024)

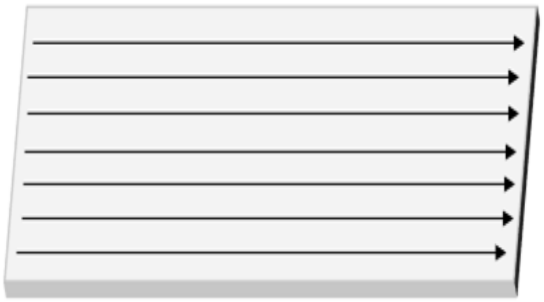

Figure 4.4. Singular direction scan pattern (Source: ANSYS 2024)

$$\varepsilon_{xx} = SSF * ASC_x * \frac{\sigma_{yield}}{E} \tag{4.5}$$

$$\varepsilon_{yy} = SSF * ASC_y * \frac{\sigma_{yield}}{E} \tag{4.6}$$

$$\varepsilon_{zz} = SSF * ASC_z * \frac{\sigma_{yield}}{E} \tag{4.7}$$

For the case of this irregular scanning strategy, *ASC* demonstrates anisotropic strain coefficients, and these variables can be different for all scanning strategies (ANSYS 2024).

4.2.1.2 Thermal Strain Scaling Factor

Thermomechanical simulations do not require the use of a strain scaling factor since all the necessary inputs to include thermal effects in the simulation should be

established before solving these simulations. However, to minimize the variation between printed parts and simulated parts, another artificial coefficient used in FEA of AM is the thermal strain scaling factor. This factor, in most cases, has the default value of 1. In specific situations, for example when an unusual material is used, or some machine parameters are unknown, or in cases where environmental variables can vary, this factor is calculated. This factor has minimal effect on the results compared to strain scaling factor.

$$\varepsilon^{total} = \varepsilon^{elastic} + \varepsilon^{thermal} + \varepsilon^{plastic} + \varepsilon^{phase} + \varepsilon^{creep} \tag{4.8}$$

Equation 4.8 demonstrates the entire scale of strains that can be calculated during a finite element analysis and the thermal strain scaling factor only applies to the calculation of $\varepsilon^{thermal}$ (ANSYS 2024).

4.3. Meshing Methodology

For FEA of AM, a method called "Lumped Layer Approach" is used. This method combines several physical layers of the manufactured part, assuming that combining these several layers would not alter the general results, and that not all layers yield different results meaning layers with similar behaviour can be grouped together, or "lumped". The motivation behind this approach is shortening the simulation time while catching the global stress, strain and deformation. Generally, lumping 10 to 20 layers is recommended and mesh is created accordingly. A single element height is recommended to take space between 10 to 20 times of a single physical layer height (ANSYS 2024).

Three different approaches exist for FEA of AM for meshing parts. First approach is creating a cartesian mesh, demonstrated in Figure 4.5. Cartesian mesher creates a hex mesh that approximates the geometry but details like small faces, curved features etc. may not be accurately captured using this method. This method requires the user to obey the 10 – 20 element size rule-of-thumb, also making sure that element size is small enough to capture bigger details of the part. This method is fast, and accuracy is adequate. This method utilizes cubic elements that can be deformed to capture the geometry.

Another option for meshing of FEA for AM is using voxels. Voxelized mesh option uses cubic elements. This method, just like the cartesian method, may not capture small details but utilizes a knockdown factor to account for the uncaught details.

Last option when it comes to meshing is the layered tetrahedrons method, demonstrated in Figure 4.6. This method creates a tetrahedron mesh and can easily capture details like small faces and curved features. This method is recommended for use with organic shapes, holes, tiny features and thin walls. While layered tetrahedrons method can capture many details with ease, this method generates more mesh elements than the other two, meaning this method requires more time and hardware in order to solve the FEA (ANSYS 2024).

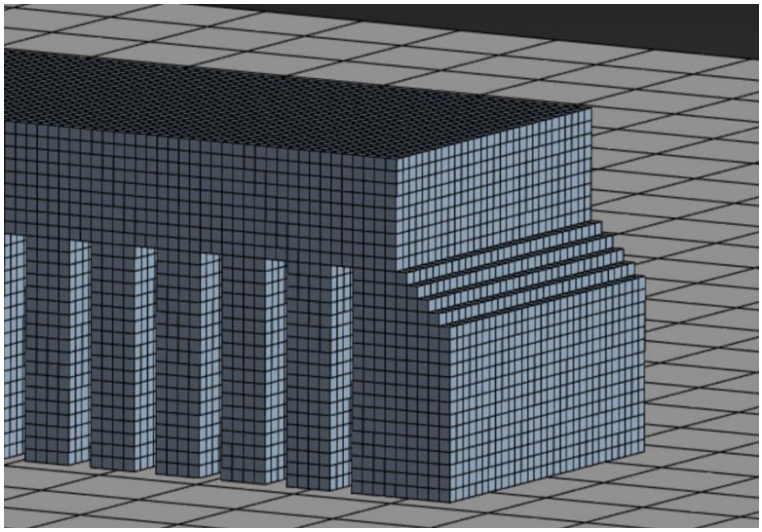

Figure 4.5. Cartesian mesh

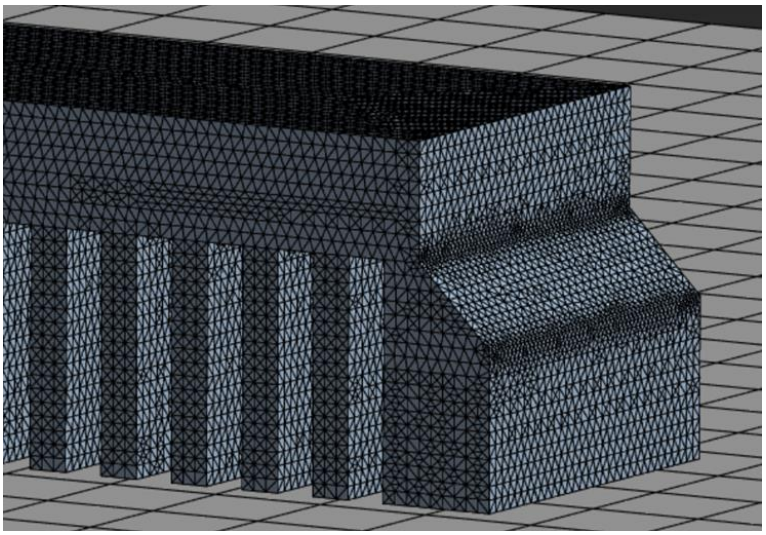

Figure 4.6. Layered tetrahedrons mesh

4.4. Material Modeling

Additive manufacturing simulations require material properties dependent or independent with temperature depending on the simulation approach. While inherent strain scenarios can be solved with no temperature dependent data, thermomechanical scenarios require in-depth temperature dependent material properties. Since many properties are required, material data for thermomechanical simulations is scarce and experimenting can be expensive. Simulation packages such as Ansys offer several commonly used materials with the FEA solver such as AlSi10Mg or Ti64. Maraging Steel, on the other hand, is not that commonly used and has unique aspects to it that makes it harder to simulate.

CHAPTER 5

RESULTS AND DISCUSSION

In this thesis study, a benchmark comb shaped part shown in Figure 5.1 has been simulated using finite element analysis. The material for these simulations was selected to be maraging steel and displacement results were compared to an existing reference study (L. Mugwagwa et al. 2018).

5.1. Problem Statement

A benchmark comb shaped geometry was printed using several different combinations of input parameters. Then, thinner legs of these printed parts were cut from the baseplate while the thicker part remained attached. This enabled the demonstration of residual stresses and strains that warped, or curved, the printed part for strain relief. The amount of deformation at the lower right-most tip of the part, which moved away from the baseplate depending on the amount of residual effects, was the output for the reference study (L. Mugwagwa et al. 2018). This deformation can be seen in Figure 5.1. Simulations in this study has the purpose of matching the same amount of deformation as recorded by the physical parts.

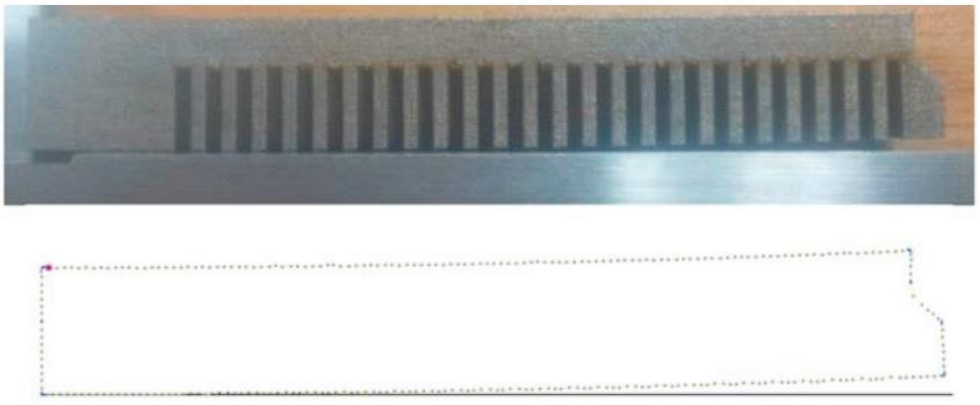

Figure 5.1. Separation from baseplate (Source: Mugwagwa et al. 2018)

5.2. Geometry Preparation

The geometry used in this study is a simple comb shaped benchmark part. The dimension for the geometry is given in Figure 5.2.

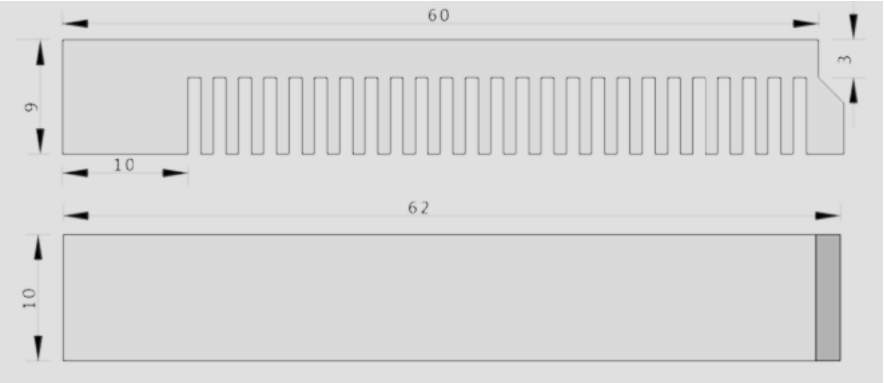

Figure 5.2. Dimensions of the benchmark part (Source: Mugwagwa et al. 2018)

This part was designed to the specified dimensions given in Figure 5.2 using ANSYS SpaceClaim. Afterwards, a baseplate (the plate where the printed part is manufactured on) with the dimensions of 125x125x5 millimetres, shown in Figure 5.3 was drawn below the benchmark part with the parts touching each other directly.

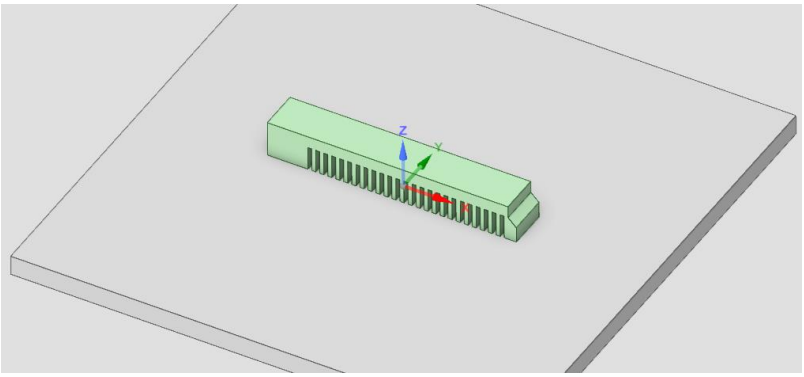

Figure 5.3. Benchmark part with baseplate

5.3. Meshing

For discretization of geometries to be used in finite element analysis of L-PBF, using element sizes between 10 to 20 times of the layer thickness is recommended

(ANSYS 2024). Since the reference study included layer heights of 30 and 45 micrometres, a uniform element size (for width and height) of 0.3 millimetres was deemed appropriate (L. Mugwagwa et al. 2018). Considering the available element technologies, given that the part in this study mainly consists of chunky geometry, a cartesian mesh with element size of 0.3 has been used. Baseplate, on the other hand, has been meshed with an element size of 3 millimetres. Mesh quality parameters can be found on Table 5.1. As it can be seen on Table 5.1, cartesian method created a near ideal mesh. This mesh size yielded results with good convergence.

Table 5.1. Mesh quality parameters

Mesh Quality Parameter	**Parameter Value**
Minimum Element Quality	0.98077
Maximum Element Quality	1
Average Element Quality	0.99946
Standard Deviation of Element Quality	0.0031786

5.4. Material Modeling of Maraging Steel

Maraging steel and similar materials are alloys consisting of iron, nickel, and cobalt with additional titanium, aluminium, and molybdenum. They are employed in industry where ductility along with great strength and toughness are required. Maraging steel during AM cools and changes from austenite to martensite in its solid-state phase. The material properties need to take the phase change into account for simulation package to accurately represent the phenomena. To account for the phase change, a beta extension of Ansys has been used. Maraging steel has the melting temperature of 1413 °C, which is also assumed to be the zero thermal strain temperature where the material is assumed to dissipate any inherent strains. The Maraging Steel Beta Tool can only be used with thermomechanical simulations and comes with material data for both austenite and martensite phases of maraging steel. These data, except for the Poisson's ratio which is assumed to be 0.3, is highly dependent on temperature, hence temperature dependent mechanical properties are utilized. The temperature dependent data for both stages can be found on Table 5.2.

Mechanical Properties of Maraging Steel

Density (kg/m^3)	Young's Modulus (GPa)	Yield Strength (MPa)	Tangent Modulus (MPa)	Thermal Conductivity (W/m. °C)	Coefficient of Thermal Expansion (1/°C)	Specific Heat Constant Pressure (J/kg. °C)
8100 (at 20 °C)	150 (at 199 °C)	1050 (at 199 °C)	3000 (at 199 °C)	14.2 (at 20 °C)	1.1×10^{-5} (at 20 °C)	452 (at 20 °C)
7865 (at 1000 °C)	180 (at 200 °C)	433 (at 200 °C)	754 (at 200 °C)	21 (at 600 °C)	1.2×10^{-5} (at 199 °C)	544 (at 300 °C)
	173 (at 400 °C)	296 (at 816 °C)	339 (at 816 °C)	28.6 (at 1300 °C)	1.55×10^{-5} (at 200 °C)	655 (at 500 °C)
	164 (at 500 °C)	80 (at 1040 °C)	194 (at 1040 °C)			826 (at 700 °C)
	155 (at 600 °C)	39 (at 1150 °C)	127 (at 1150 °C)			887 (at 900 °C)
	144 (at 700 °C)					
	131 (at 800 °C)					
	117 (at 900 °C)					
	100 (at 1000 °C)					
	81 (at 1100 °C)					
	51 (at 1200 °C)					

Table 5.2. Mechanical properties of maraging steel (ANSYS 2024)

5.5. Simulation and Calibration

Every thermomechanical simulation for this study has been conducted with the same software and hardware combination. Ansys 2024 R1 software package along with Intel Xeon W-1350P @4.00 GHz with 6 cores, 128 GB of RAM and a 1 TB Samsung SSD hardware specifications have been used. All simulations were solved on 6 cores using Shared Memory Parallel method due to the limitations of the beta-stage maraging steel tool.

FEA solution consisted of 3 load steps. The first load step had the part being built layer by layer, following a chessboard scanning pattern utilizing the formulas given in Equations 4.2, 4.3 and 4.4, and was formed by 54 substeps. Second load step was the cooldown step where the part was solved for cooling down via convection. This step consisted of 21 substeps. The last step was where the separation, or cutting, from the baseplate took place. The solver was programmed to cut the part in 4 substeps. A sequence scheme for these steps can be found in Figure 5.4, where the User Step under the Static Structural title is when cutting from baseplate takes place.

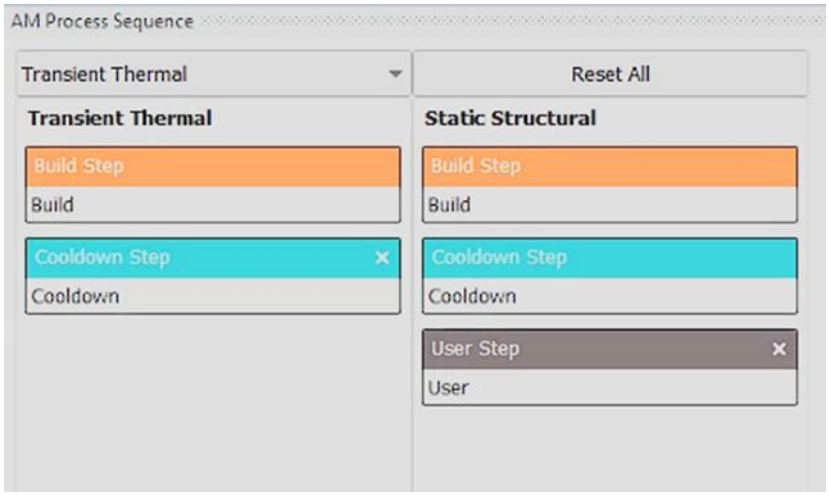

Figure 5.4. Sequence scheme for FEA

The cutting operation was done using the “Contact Step Control” option of Ansys Mechanical. This option allows certain contacts to be “killed” or “birthed” during certain steps. The contact between the part and baseplate was created accordingly, and this contact where the thinner comb legs touch the baseplate was “killed” one by one during

the third load step of this simulation. The thicker comb part was left in contact with the baseplate, as it was for the physical measures.

Before solutions, thermal strain scaling factor was defined as an input parameter and directional deformation on the print direction at the tip of the calibration part was defined as an output parameter. In order to match physical results as accurately as possible, only the deformation at the Z direction, which is the directions the part was being built at was taken as the single output parameter.

Other parameters (layer thickness, laser power and scanning speed) were defined as constants to the software, and each parameter combination was created as a single simulation study. This meant that this study had 37 distinct simulation models. Existing combinations of these parameters can be found in Figure 5.5 while exemplary distinct simulation models can be found in Figure 5.6.

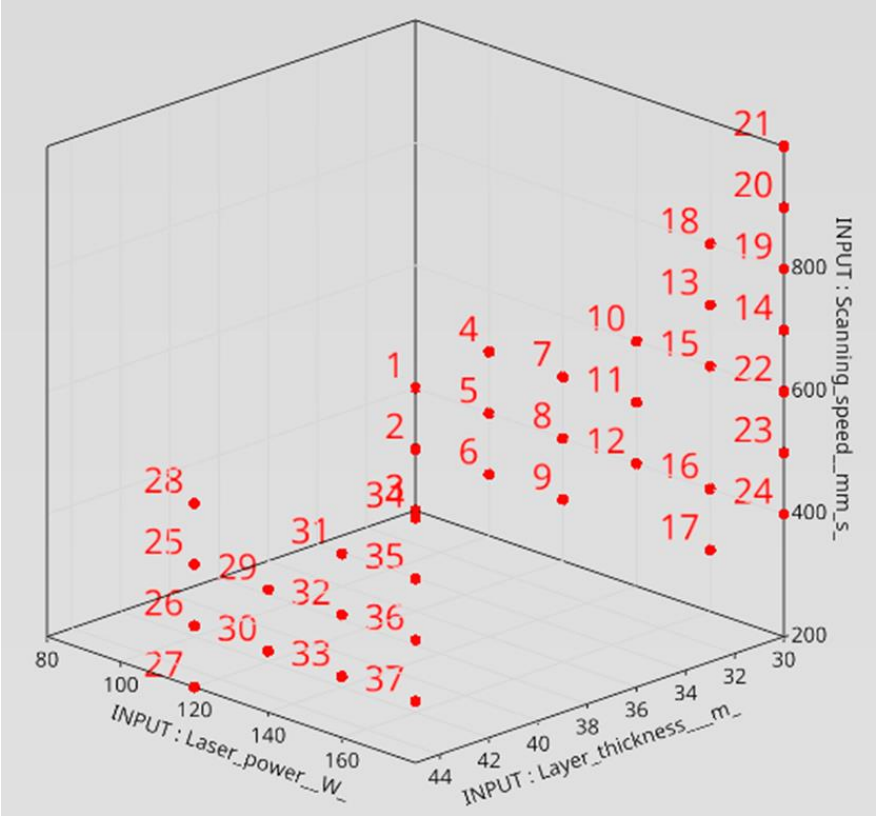

Figure 5.5. Combinations of parameters

Thermomechanical simulations can yield different results from physical parts because many simulations are estimations of physical processes and not all parameters during the manufacturing process can be accounted for. To overcome this, thermal strain

scaling factors for all distinct simulation models have been calculated using direct optimization methods.

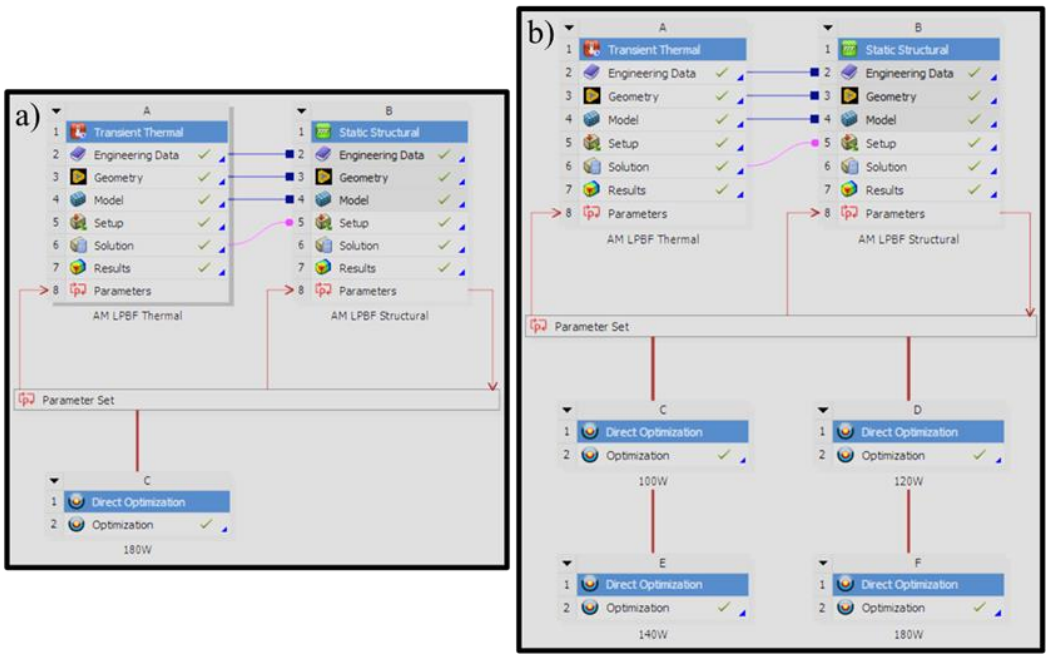

Figure 5.6. a) Simulation model for the 30 micrometres, 200 mm/s combination only had 1 model while b) 30 micrometres, 500 mm/s combination had 4 distinct models

Table of Schematic C2: Optimization

	A	B	C	D	E	F	G	H	I
1	Name	Parameter	Objective			Constraint			
2			Type	Target	Tolerance	Type	Lower Bound	Upper Bound	Tolerance
3	Seek P2 = 0.74 mm	P2 - Directional Deformation Average	Seek Target	0.74	0.001	No Constraint			
*		Select a Parameter							

Table of Schematic C2: Optimization

	A	B	C	D
1	Input Parameters			
2	Name	Lower Bound	Upper Bound	
3	P1 - Build Settings Thermal Strain Scaling Factor	0	3	
4	Parameter Relationships			
5	Name	Left Expression	Operator	Right Expression

Figure 5.7. TSSF range and "Seek Results" command for 30 micrometres, 500 mm/s at 100 W combination

Direct optimization over the DoE data has been used to calculate thermal strain scaling factor of each simulation model. The reference study included the separation of

the tip of the part from the baseplate for each sample combination (L. Mugwagwa et al. 2018). Considering this data was given, what should be calculated as the directional deformation, or separation from the baseplate, at the tip of the benchmark part was given to the software as the target with a tolerance of 0.001. Only variable the software could change during this approximation was the thermal strain scaling factor, with the default value taken as 1.

A range of 0 to 3 was defined as the initial range for the thermal strain scaling factor. Adaptive Single-Objective method was used as the DoE optimizer. Initial number of samples was set as 5, maximum number of evaluations was set as 22 and maximum number of candidates was set as 3 as can be seen in Figure 5.8.

Properties of Outline A2: Optimization

	A	B
1	Property	Value
2	Design Points	
3	Preserve Design Points After DX Run	☐
4	Failed Design Points Management	
5	Number of Retries	0
6	Optimization	
7	Method Selection	Manual
8	Method Name	Adaptive Single-Objective
9	Estimated Number of Design Points	22
10	Tolerance Settings	☑
11	Number of Initial Samples	5
12	Maximum Number of Evaluations	22
13	Convergence Tolerance	1E-06
14	Maximum Number of Candidates	3
15	Optimization Status	
16	Converged	No
17	Number of Design Points	0
18	Number of Domain Reductions	0
19	Number of Failures	0
20	Size of Generated Sample Set	0
21	Number of Candidates	0
22	Design Point Report	
23	Report Image	None

Figure 5.8. Settings for direct optimization engine

All models were subjected to the optimization engine individually and candidates were attained. Convergence of the thermal strain scaling factor for some models can be found in Figures 5.9, 5.10 and 5.11. Initial range of 0 to 3 for the thermal strain scaling

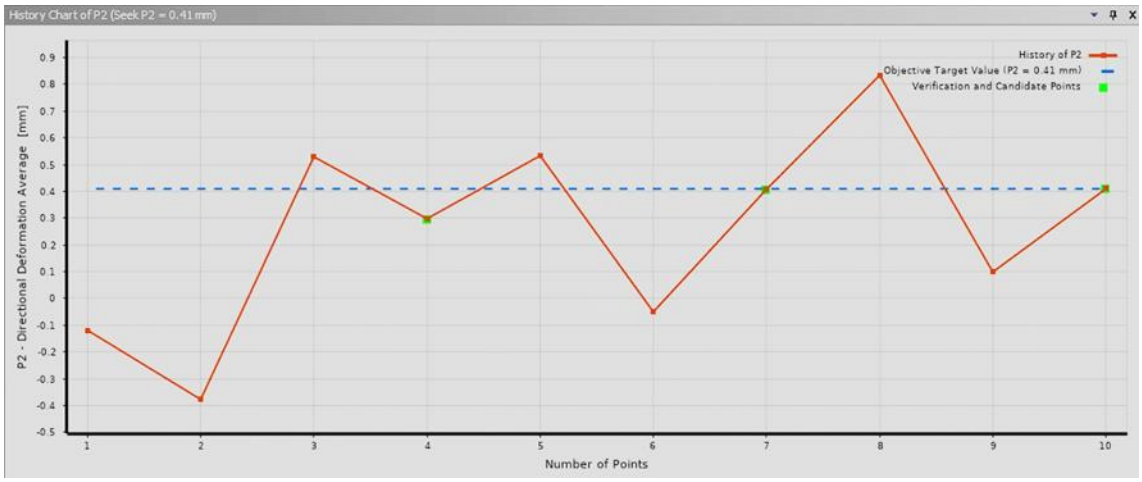

Figure 5.9. Convergence graph of 45 micrometres, 500 mm/s and 140 W combination

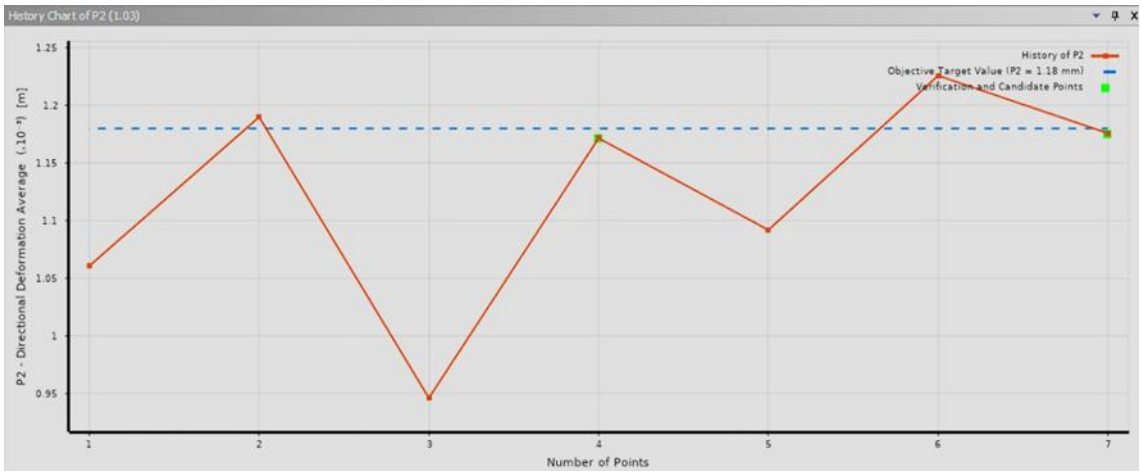

Figure 5.10. Convergence graph of 30 micrometres, 1000 mm/s and 180 W combination

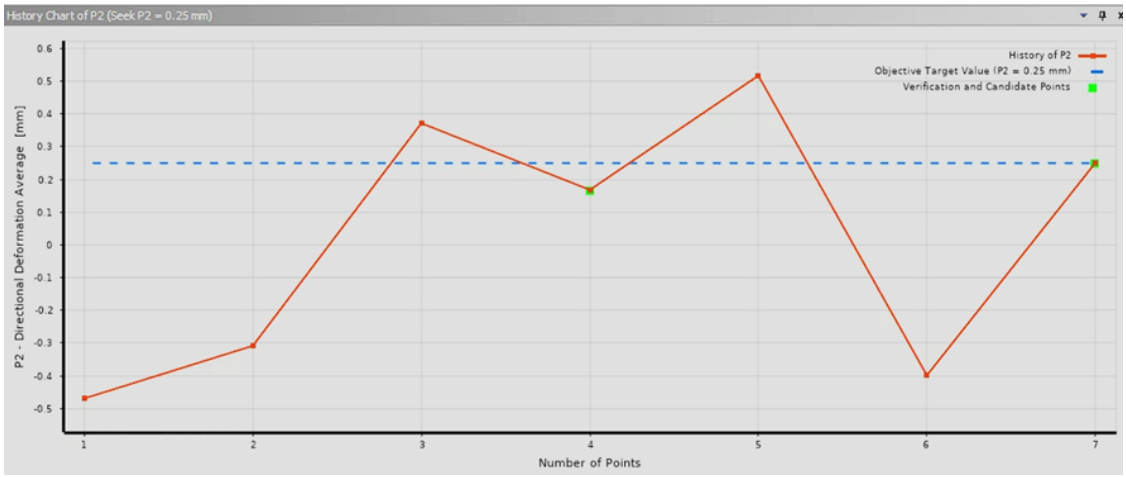

Figure 5.11. Convergence graph of 45 micrometres, 200 mm/s and 120 W combination

factor has been altered for several of the design points in order to attain correct coefficients. All models were successfully calculated, or calibrated, to yield thermal strain scaling factors where deformations of the physical samples could be met. See Appendix A for a table of thermal strain scaling factors calculated for each distinct simulation model.

5.6. Stochastic Optimization of Simulation Results

Since a DoE study was already conducted on the existing data in order to calibrate the simulation, a software package called OptiSlang 24R1 was utilized to extract the metamodel of optimal prognosis of the direct optimization, or the calibration study. For the MOP; laser power, layer thickness and scanning speed taken from the reference study were given as inputs. Thermal strain scaling factors gained from the direct optimization study were also given to the software as inputs. Maximum distortion calculated during the simulations were taken as the output. Since the directional deformation at the print direction, or the separation from the build plate, are the same for both calibration and the reference study, this was taken as a single parameter, hence the output (L. Mugwagwa et al. 2018).

MOP creation was done using the Excel plug-in of OptiSlang. One of the first outputs of the MOP was the correlation matrix, shown in Figure 5.12. A correlation matrix is a representation of the correlations between several variables. Two variables' correlation coefficient is represented by each cell in the matrix. When one variable grows, the other increases proportionately, or in a perfect positive correlation, which is shown by a correlation coefficient value of +1. The correlation coefficient has values ranging from -1 to +1. When one variable rises, the other falls proportionately, and this is known as a perfect negative correlation, which has a value of -1. No linear association exists between the variables when the value is 0.

When a variable is perfectly correlated with itself, its diagonal elements, which show how each variable relates to itself, always equal 1.

Another output of the MOP is the histogram. A histogram is a kind of graphical representation that shows the distribution of numerical data. It is made up of bars whose heights represent the proportion of observations that fall into each of a set of adjacent intervals, sometimes referred to as buckets or bins.

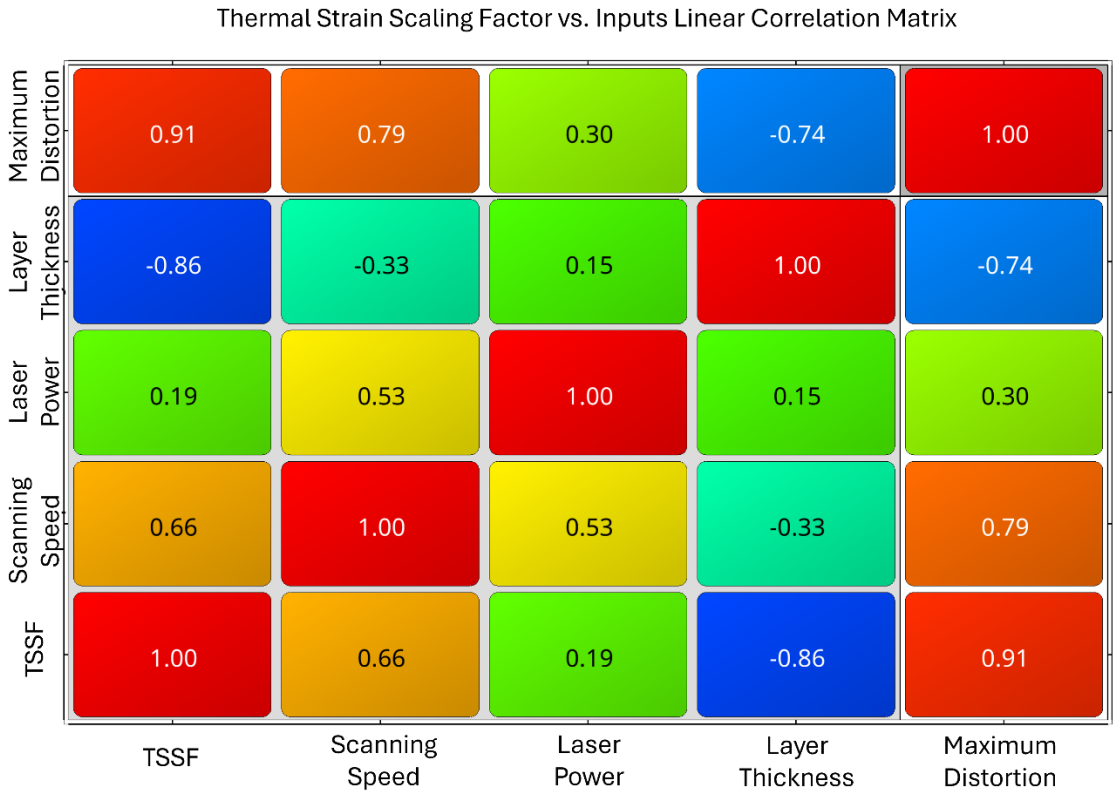

Figure 5.12. Correlation matrix

Patterns, trends, and possible outliers in the data are easily discernible since the area of each bar is proportionate to the number of observations inside the interval it represents. Figure 5.13 represents the histogram data for the thermal strain scaling factor, showing that values between 0 to 0.5 had the highest frequency of appearance.

According to the MOP, when the distortion from DoE is submitted to a linear regression approximation model, coefficient of prognosis, which typically refers to a statistical measure used to understand the predictive accuracy or reliability of a prognostic model, yielded a result of 91%. This shows that the calculated MOP has a high accuracy of prediction and can be used for further investigative studies to determine new values for distortion. Figure 5.14 represents the 3D response surface plot where input and output combinations of the DoE study are mapped on a 3D plot for visualization.

To accommodate the fitness of the response surface, the residuals, or errors, from a regression analysis or other prediction models are displayed graphically in statistical analyses using a residual plot. The difference between each data point's observed value and its anticipated value by the model is used to compute residuals.

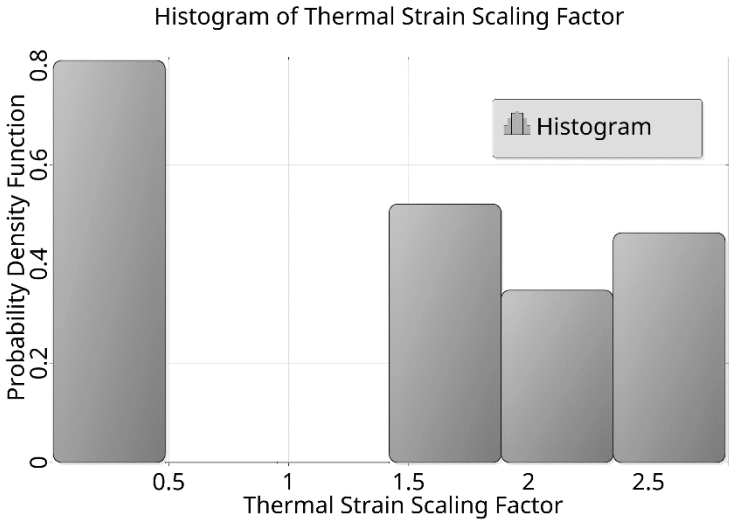

Figure 5.13. Histogram of thermal strain scaling factor

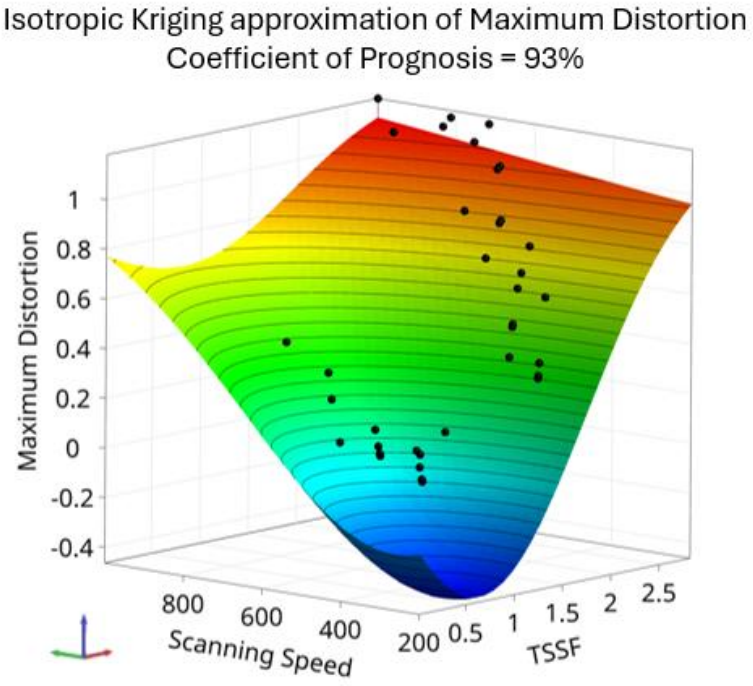

Figure 5.14. 3D response surface plot

A residual plot, given in Figure 5.15 is used to evaluate a model's quality of fit and validate the basic assumptions of the regression study. In particular, it's employed to identify data patterns that the model would have missed. Here, data points for both fitting and prediction are supposed to not be far away from each other to prove a good fit.

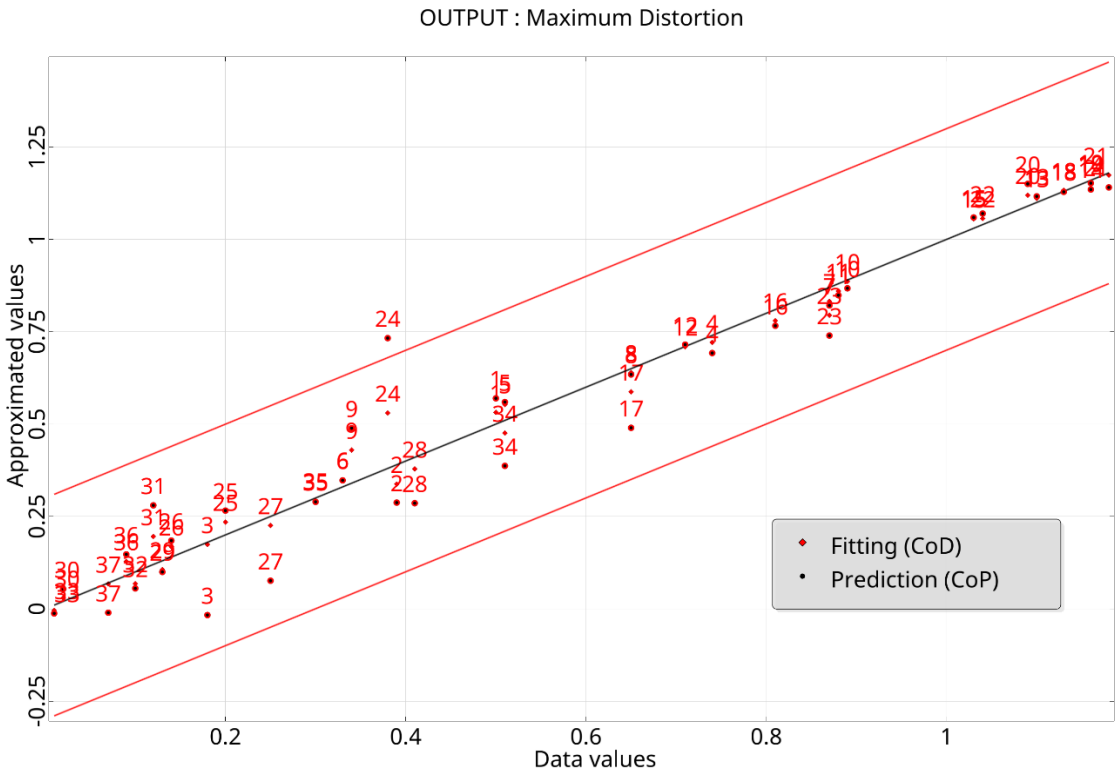

Figure 5.15. Residual plot

Coefficient of Prognosis (CoP) is a model independent measure to assess model quality in optimization, shown in Equation 5.1:

$$CoP = 1 - \frac{SS_E^{Prediction}}{S_T} \tag{5.1}$$

Where the nominator is the sum of squared prediction errors, and the denominator is the total variation of the output. The cross-validation method is used to estimate these errors. The set of support points is translated to a determinate number of subsets in the cross-validation process. A single subset is then eliminated from the support points, and the remaining point set is used to approximate the subset model output in order to construct the approximation model. This indicates that only at the subsets where the approximation model is not constructed is the model quality estimated. This strategy is applicable to both regression and interpolation models, as the prediction error is utilized instead of the fit. The computation of the CoP requires additional computational work due to the examination of the cross-validation subsets, which are typically between 5 and 10 sets (ANSYS 2024).

As it can be observed from Figure 5.16, while the thermal strain scaling factor, an artificial coefficient that was added for this study, has a higher percentage of CoP than laser power, a physical input parameter that directly affects the printed part, the effect of these parameters are quite different on the actual output. Similarly, looking at Figure 5.12, the correlation matrix from the MOP demonstrates that deflection and scanning speed have a high rate of positive correlation. Figure 5.16 further demonstrates this relationship by showing that scanning speed has a high rate of CoP. Layer thickness on the other hand demonstrates a high rate of negative correlation with deflection while maintaining a strong effect on the output regardless of the sign of the correlation.

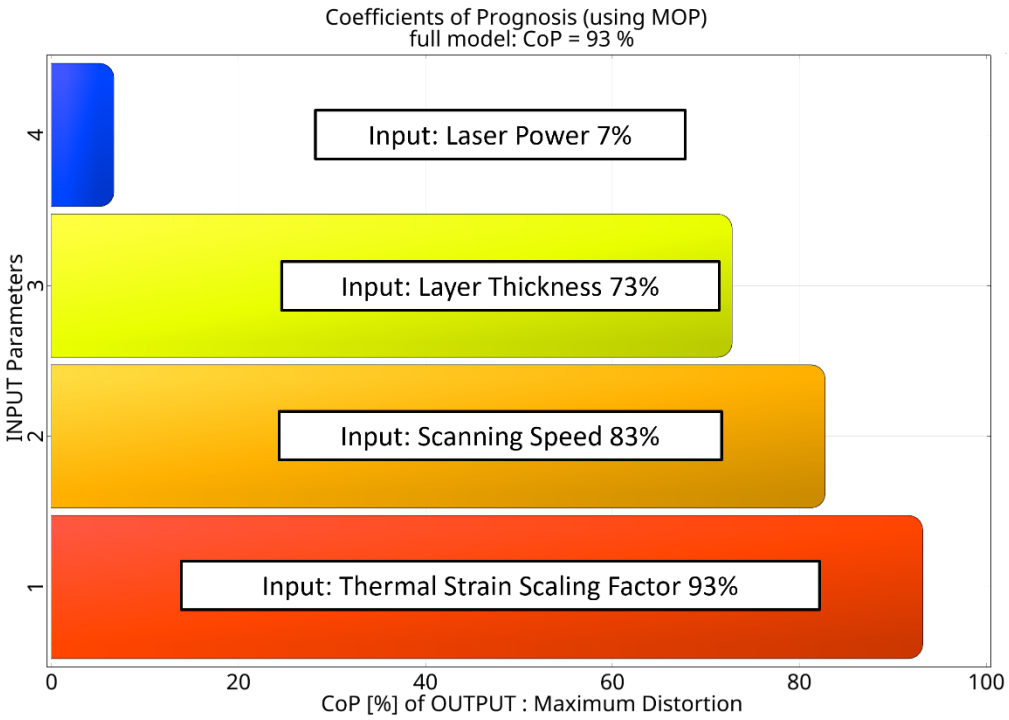

Figure 5.16. Coefficient of prognosis

After the calculation of MOP, the metamodel was sent to a stochastic optimization solver, specifically the evolutionary algorithm solver in OptiSlang. While setting up the EA, the testing type was set as “Cross validation”. Tested metamodels option was set to “Polynomial + MLS + Kriging”. Variable reduction option was set to “No reduction”. This meant that design points would be cross validated for the EA, several metamodel extraction methods would be utilized and even if some parameters were found to be unimportant, they would not be reduced, meaning all parameters would exist in the EA

regardless of importance or sensitivity. A screenshot of this setup can be found in Figure 5.17.

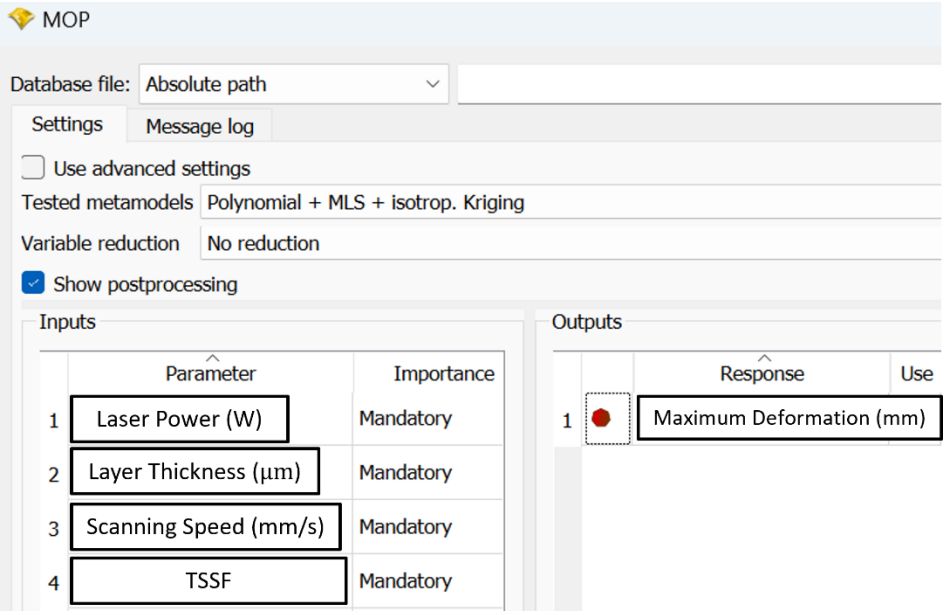

Figure 5.17. MOP data transfer settings

Some inputs were necessary for this solver, starting with the input parameters. Input parameters (thermal strain scaling factor, scanning speed, layer thickness and laser power) were forwarded directly from the MOP. Ranges for these parameters were taken from the direct optimization study. Specifically, for the layer thickness parameters, as only two values existed (30 and 45 micrometers of layer thickness), this parameter was introduced to the EA solver as nominal discrete while other parameters were introduced as continuous within their respected ranges, as can be seen in Figure 5.18.

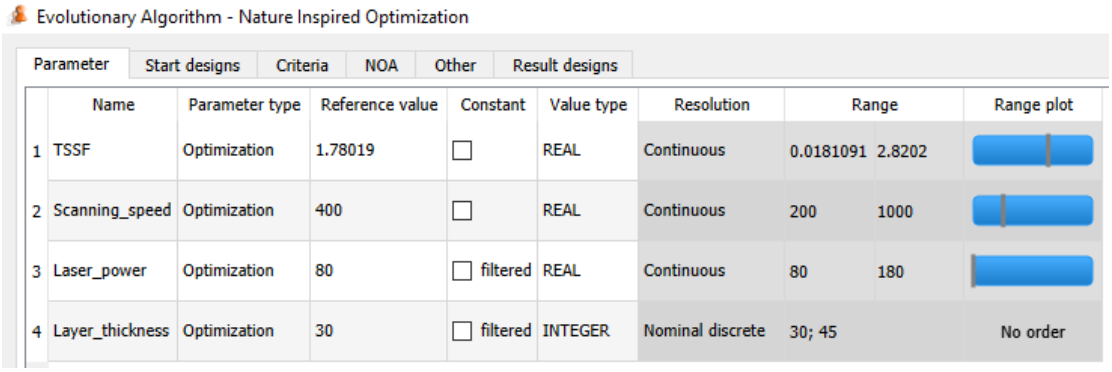

	Name	Parameter type	Reference value	Constant	Value type	Resolution	Range		Range plot
1	TSSF	Optimization	1.78019	☐	REAL	Continuous	0.0181091	2.8202	
2	Scanning_speed	Optimization	400	☐	REAL	Continuous	200	1000	
3	Laser_power	Optimization	80	☐ filtered	REAL	Continuous	80	180	
4	Layer_thickness	Optimization	30	☐ filtered	INTEGER	Nominal discrete	30; 45		No order

Figure 5.18. Parameter introduction to EA

Then, start designs were introduced to the solver settings. Afterwards, the stochastic optimization problem was defined. The problem statement here was that the maximum deformation result, or separation from the build plate, were to be minimized within the acceptable data range. Considering this is a numerical solution, a limit to the criteria was added saying that the minimized deformation had to be a positive number, as seen in Figure 5.19.

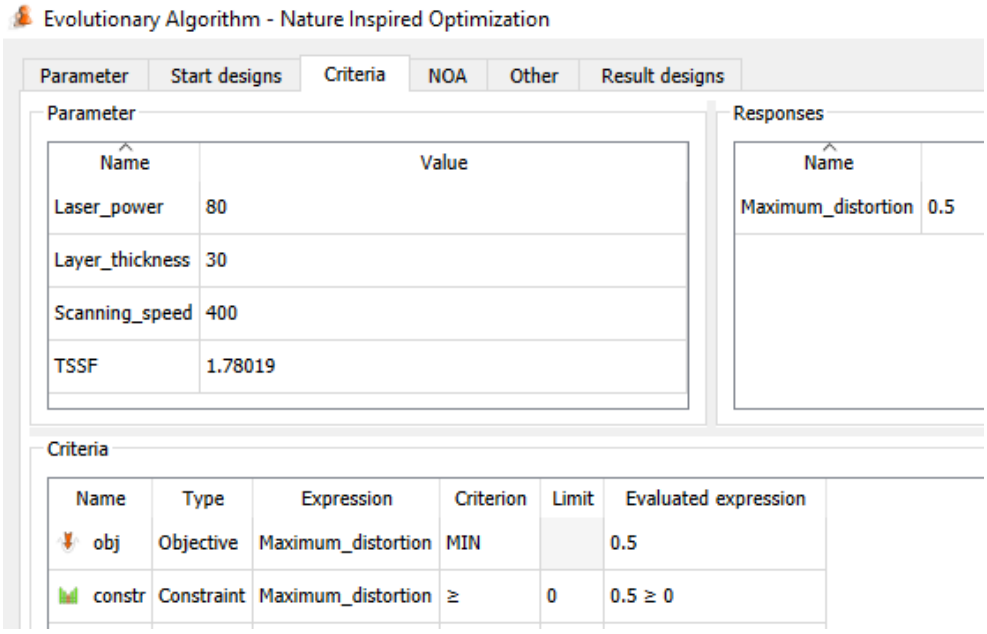

Figure 5.19. Criteria settings for EA

After the problem statement, evolutionary algorithm solver was selected. A maximum number of 10000 samples were set in the program with search strategy set to a balanced load. Balanced load meant that the starting population size for the EA was set as 10, maximum number of generations as 1000, fitness method as weighted sum, number of parents as 5, ranking method as linear, selection method as stochastic and crossover probability as %50.

Aforementioned settings were given to the EA and results were gained through OptiSlang. The evolutionary algorithm solver yielded 480 different design points. During this process, the solver engine was kept calculating for 48 different generations and 28th generation yielded the best results. There were a total of 316 feasible design points and 272nd design point, part of the 28th generation, was selected as the best design.

Looking at a plot of thermal strain scaling factors, at Figure 5.20, a general idea of successful and failed generations can be visualized. According to this history plot, while the EA initially tried a wide range for TSSF, values around 1.5 yielded the best results including the best generation.

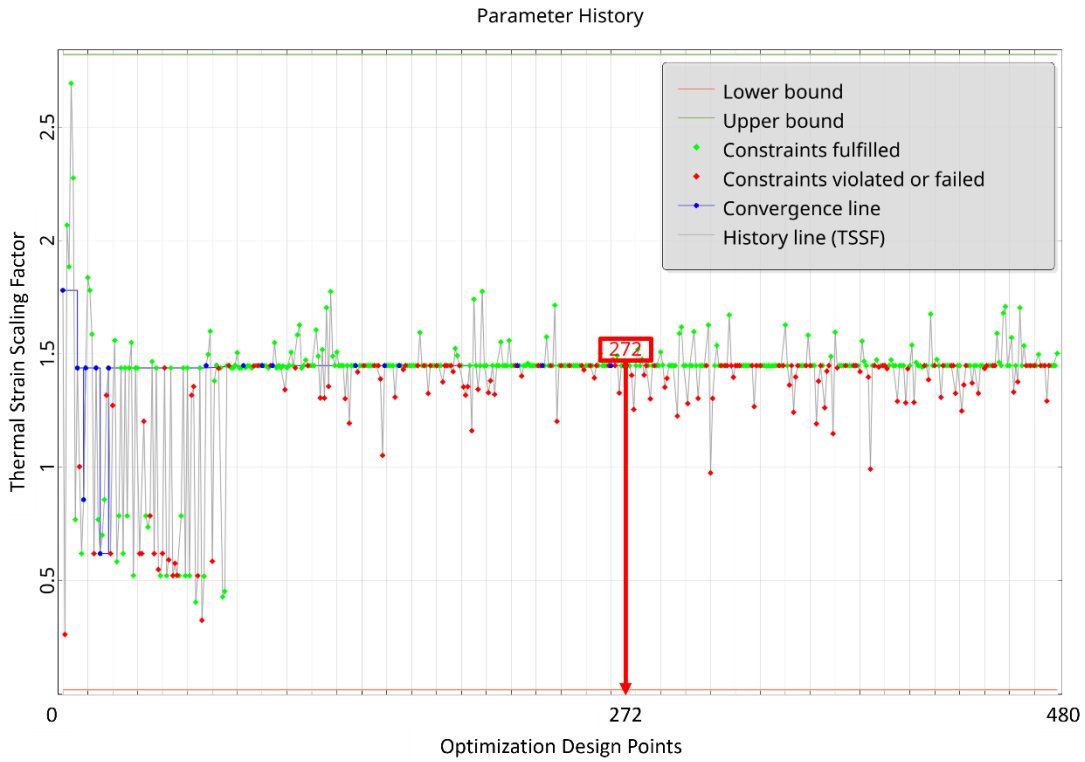

Figure 5.20. Parameter history plot of thermal strain scaling factor

Figure 5.21 on the other hand represents a history plot of scanning speed over design points. A steep drop in in speed after several iterations can be observed as the EA moved forward with newer generations, implying that while scanning speeds around 800 mm/s yielded good results for the initial generations, optimum results were achieved at newer generations with lower speeds, around 200 to 300 mm/s. Scanning speed values in the range of 300 to around 400 milimetres per second yielded relatively lower ratio of successful iterations and were not favoured by the optimization engine.

Laser power of around 150 Watts yielded good results, but a trend of slight increase as the EA generated newer iterations can be observed in Figure 5.22. The slight increase in laser power as newer generations were created indicates that while the optimization was calculating design iterations, a decrease in deflection was observed with larger amounts of laser power and this behaviour further encouraged the increase in laser power for the newer generations. The trend of slight increase was diminished at

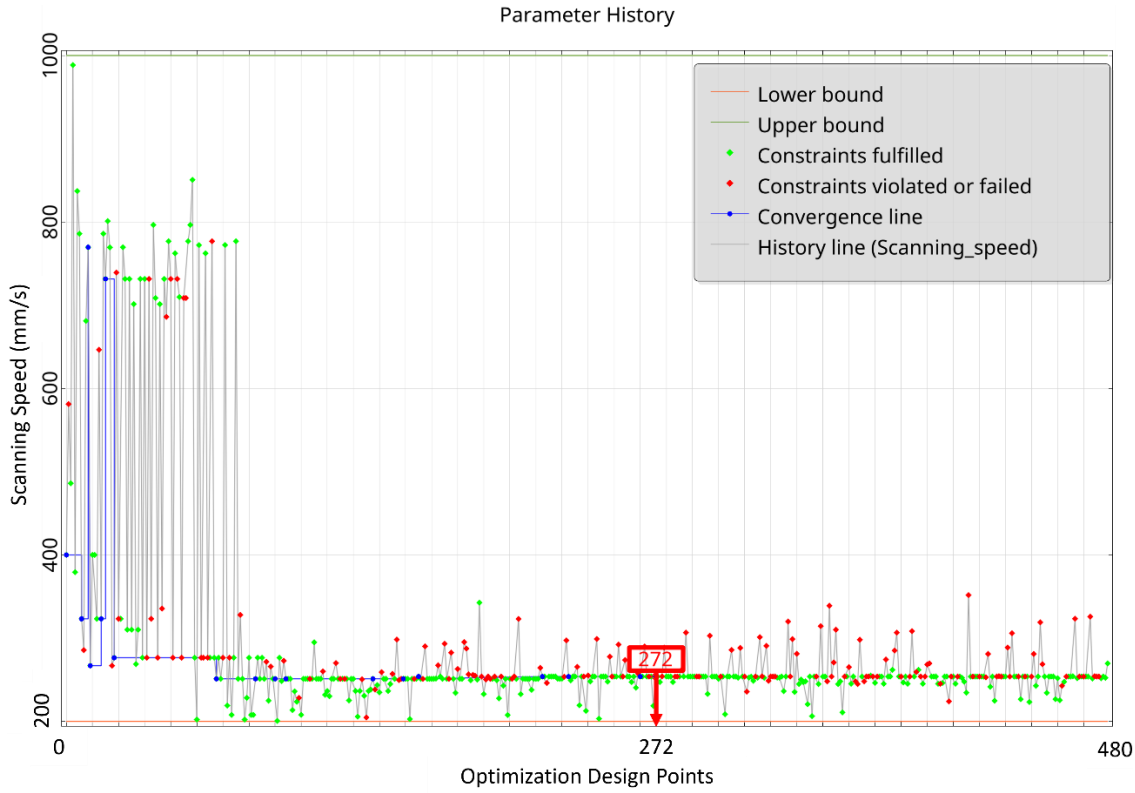

Figure 5.21. Parameter history plot of scanning speed

Figure 5.22. Parameter history plot of laser power

around half point of the generations created as the optimum point was reached and the optimization engine tested out different values in the 140-160 Watts range until the calculation was concluded. The optimum generation had the laser power of 150.843 Watts.

5.7. Best Generation Specifications

The best candidate, namely the 272nd design point, had the following specifications, given in Figure 5.23.

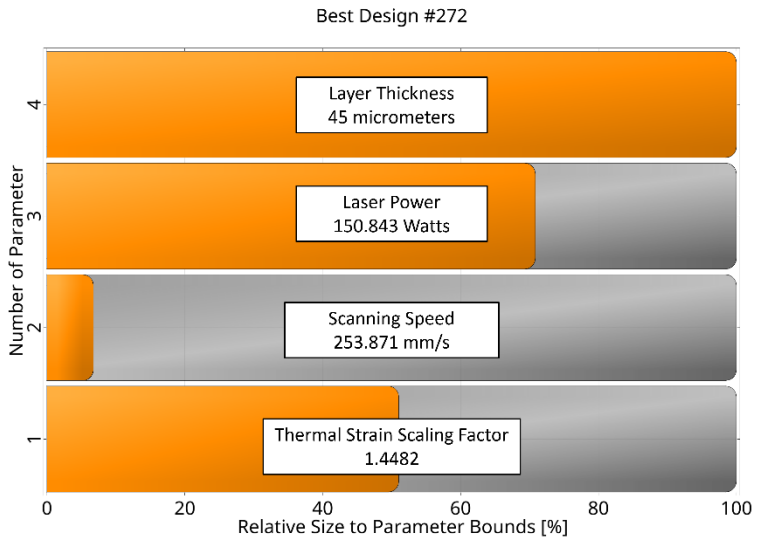

Figure 5.23. Parameters of best design

According to the EA, a combination of 45 micrometres of layer height, 150.843 Watts of laser power and 253.871 mm/s scanning speed would yield the minimum amount of deformation for the benchmark part and a thermal strain scaling factor of 1.4482 could be used to simulate this combination and similar combinations beforehand.

The best, or 272nd, design point yields a deformation, or separation from baseplate, at a value of $6.283*10^{(-5)}$ millimetres. This result is quite low and could potentially be assumed to be zero.

5.8. Successful Generations

Examining the output deformation results, some important assumptions could be made. One key assumption could be that if any of the results show a deformation smaller

than one thousandth of a millimetre, which is also known as a micrometre, that amount of deformations could be considered to be zero. This meant that even if there exists a very small amount of deformation, as long as the yielded result is less than a micrometre, the parameter combination could be assumed to be successful.

Making this assumption can help simplify the data and results. This process of treating very small deformations as zero could allow more effective filtering of results. As a result of this assumption, many more successful combinations of parameters can be found. These successful combinations can be important because they make it possible to use other parameter combinations than the best design. It could prove difficult to replicate the 272nd design point for every L-PBF machine, due to the limits of each and every machine has. So, by assuming that deformations smaller than a micrometre were zero, more successful combination parameters can be gained and used for successful metal AM of maraging steel.

The EA used in this study yielded 480 distinct design points and out of those design points, 51 different design points, including the 272nd yielded deformation results that were smaller than a micrometre. See Appendix B for design points yielding deformations smaller than a micrometre and their respective parameter combinations.

CHAPTER 6

CONCLUSION

In this thesis, inputs and outputs shared by a reference study where maraging steel parts were additively manufactured have been simulated using thermomechanical finite element analysis simulation approach, and thermal strain scaling factors have been calculated with a direct optimization method to provide a precise convergence between printed parts and simulated parts (L. Mugwagwa et al. 2018). Then a stochastic optimization method was utilized to solve and predict many other parameter combinations for ideal manufacturing parameters of maraging steel.

Metal additive manufacturing of maraging steel can yield hard to predict results because of the low phase change temperatures of maraging steel. This material is both hard to manufacture and simulate. Previous studies include metal additive manufacturing parameters of several different combinations for maraging steel along with deformation results of utilized parameter sets (L. Mugwagwa et al. 2018). These parameter sets were introduced to finite element analysis in order to gain matching results from both simulations and physical tests. These finite element simulations made use of a thermomechanical approach where every layer, quite similar to the actual AM process, were simulated by creating mesh elements of a layer at the melting temperature and then solving for the thermal and mechanical strains while the layer solidified. This process was repeated layer by layer until the comb shaped benchmark part was completed.

An unusual material introduction method was used in this study which introduced maraging steel's martensite and austenite phases as the same temperature dependent material but allowed for phase transformation if the material had spent a predetermined amount of time at the phase change temperature. This material method was incorporated to the calculation of every mesh node, and each element had the possibility to go through phase transformation at any point of the simulation if suitable conditions existed.

Considering metal AM has many parameters and is a complex process, a variable was added to the finite element analysis called the strain scaling factor. This factor, along with the FEA was subjected to a direct optimization algorithm. This algorithm was given the results for any of the parameter combinations the physical tests would yield. From there, the algorithm optimized the finite element analysis using the strain scaling factor

and created trial and error simulations until FEA yielded almost perfectly matching results to the physical tests.

Having calibrated the FEA model with the physical data, these simulations were then taken to a stochastic optimization engine to solve and predict parameter combinations for an even better output of deformation. An evolutionary algorithm was utilized with the settings shared in Chapter IV.

Despite the complex nature of additively manufacturing maraging steel, getting near-ideal parts with this material was found to be possible. Also, due to the low phase change temperature characteristic of maraging steel, this material was difficult to simulate and thus, it proved difficult to predict the result of metal additive manufacturing. Making use of existing literature, simulation technology, a material model with phase change data and stochastic optimization methods, this study was able to create successful metal additive manufacturing simulations and parameter combinations for maraging steel. Throughout this study, both finite element analysis, phase changing material modeling and evolutionary algorithm proved themselves beneficial in additive manufacturing of maraging steel.

Additionally, while this thesis study primarily focuses on faults in metal additive manufactured parts caused by residual effects, failure modes such as blade crash or hot-spot defects may occur. Thanks to the calibrated FEA model, other potential failure modes could also be predicted and prevented with the method presented.

REFERENCES

Ahn, D. 2021. "Directed Energy Deposition (DED) Process: State of the Art." *International Journal of Precision Engineering and Manufacturing-Green Technology* 8, no. 2: 703-742. https://doi.org/10.1007/s40684-020-00302-7.

Ali, M. H., and Y. S. Han. 2023. "A Finite Element Analysis on the Effect of Scanning Pattern and Energy on Residual Stress and Deformation in Wire Arc Additive Manufacturing of EH36 Steel." *Materials* 16, no. 13: 4698. https://doi.org/10.3390/ma16134698.

Altıntaş, H., and H. S. Artem. 2021. "Optimization of Buckling Behavior of Hybrid Composite Beam Under Axial Compression." Master's thesis, İzmir Institute of Technology. https://hdl.handle.net/11147/11989.

ANSYS. 2024. *ANSYS User Manual*. Release 2024 R1.

Baier, O., and G. Witt. 2014. "Functional Components Produced by Multi-Jet Modelling Combined with Electroforming and Machining." *South African Journal of Industrial Engineering* 25: 182-192. https://doi.org/10.7166/25-2-659.

Bathe, K. 1996. *Finite Element Procedures in Engineering Analysis*.

Bikas, H., P. Stavropoulos, and G. Chryssolouris. 2016. "Additive Manufacturing Methods and Modelling Approaches: A Critical Review." *The International Journal of Advanced Manufacturing Technology* 83, no. 1: 389-405. https://doi.org/10.1007/s00170-015-7576-2.

Boland, T., T. Xu, B. Damon, and X. Cui. 2006. "Application of Inkjet Printing to Tissue Engineering." *Biotechnology Journal* 1, no. 9: 910-917. https://doi.org/10.1002/biot.200600081.

Bozyiğit, B., M.A. Oymak, E. Bahçe, and Ö.F. Uzunyol. 2023. "Finite Element Analysis of Lattice Designed Lumbar Interbody Cage Based on Additive Manufacturing." *Proceedings of the Institution of Mechanical Engineers, Part H: Journal of Engineering in Medicine* 237, no. 8: 991-1000. https://doi.org/10.1177/09544119231184379.

Cacace, S., and Q. Semeraro. 2021. "Fast Optimisation Procedure for the Selection of L-PBF Parameters Based on Utility Function." *Virtual and Physical Prototyping* 17, no. 2: 125-137. https://doi.org/10.1080/17452759.2021.1998871.

Castellazzi, G., A. M. D'Altri, G. Bitelli, I. Selvaggi, and A. Lambertini. 2015. "From Laser Scanning to Finite Element Analysis of Complex Buildings by Using a Semi-Automatic Procedure." *Sensors* 15, no. 8: 18360-18380. https://doi.org/10.3390/s150818360.

Castillo-Rivera, S., J. De Antón, R. del Olmo, J. Pajares, and A. López-Paredes. 2020. "Genetic Algorithms for the Scheduling in Additive Manufacturing." *International Journal of Production Management and Engineering* 8, no. 2: 59-63. https://doi.org/10.4995/ijpme.2020.12173.

Cesarano, J. III, B. H. King, and H. B. Denham. 1998. "Recent Developments in Robocasting of Ceramics and Multimaterial Deposition." United States. https://www.osti.gov/servlets/purl/290950.

Chen, S. 2019. *Investigation of FEM Numerical Simulation for the Process of Metal Additive Manufacturing in Macro Scale*. PhD diss., Université de Lyon. https://tel.archives-ouvertes.fr/tel-02402859.

Chia, H. Y., X. Wang, and W. Yan. 2022. "Process Parameter Optimization of Metal Additive Manufacturing: A Review and Outlook." *Journal of Materials Informatics* 2, no. 4: 16. http://dx.doi.org/10.20517/jmi.2022.18.

Chryssolouris, G. 2006. *Manufacturing Systems: Theory and Practice*. 2nd ed.

Depboylu, F. N., E. Yasa, O. Poyraz, and F. Korkusuz. 2023. "Thin-Walled Commercially Pure Titanium Structures: Laser Powder Bed Fusion Process Parameter Optimization." *Machines* 11, no. 2: 272. https://doi.org/10.3390/machines11020272.

Derby, B. 2015. "Additive Manufacture of Ceramics Components by Inkjet Printing." *Engineering* 1, no. 1: 113-123. https://doi.org/10.15302/J-ENG-2015014.

Durakovic, B. 2017. "Design of Experiments Application, Concepts, Examples: State of the Art." *Periodicals of Engineering and Natural Sciences* 5: 421-439. https://doi.org/10.21533/pen.v5i3.145.

Frazier, W. E. 2014. "Metal Additive Manufacturing: A Review." *Journal of Materials Engineering and Performance* 23, no. 6: 1917-1928. https://doi.org/10.1007/s11665-014-0958-z.

Gibson, I., D. Rosen, B. Stucker, and A. Khorasani. 2020. *Additive Manufacturing Technologies*. https://doi.org/10.1007/978-3-030-56127-7.

Giorgetti, A., N. Baldi, M. Palladino, F. Ceccanti, G. Arcidiacono, and P. Citti. 2023. "A Method to Optimize Parameters Development in L-PBF Based on Single and Multitracks Analysis: A Case Study on Inconel 718 Alloy." *Metals* 13, no. 2: 306. https://doi.org/10.3390/met13020306.

Gülcan, O., K. Günaydın, and A. Tamer. 2021. "The State of the Art of Material Jetting—A Critical Review." *Polymers* 13, no. 16: 2829. https://doi.org/10.3390/polym13162829.

Herzog, T., M. Brandt, A. Trinchi, A. Sola, and A. Molotnikov. 2024. "Process Monitoring and Machine Learning for Defect Detection in Laser-Based Metal Additive Manufacturing." *Journal of Intelligent Manufacturing* 35, no. 4: 1407-1437. https://doi.org/10.1007/s10845-023-02119-y.

Hill, M., and D. Nelson. 1999. "The Inherent Strain Method for Residual Stress Determination and Its Application to a Long Welded Joint." *ASME Pressure Vessels and Piping* 318.

Huang, G., K. Wei, J. Deng, M. Liu, and X. Zeng. 2022. "High-Power Laser Powder Bed Fusion of 316L Stainless Steel: Defects, Microstructure, and Mechanical Properties." *Journal of Manufacturing Processes* 83: 235-245. https://doi.org/10.1016/j.jmapro.2022.08.066.

Huang, J., Q. Qin, and J. Wang. 2020. "A Review of Stereolithography: Processes and Systems." *Processes* 8, no. 9: 1138. https://doi.org/10.3390/pr8091138.

Kantaros, A., T. Ganetsos, and D. Piromalis. 2023. "3D and 4D Printing as Integrated Manufacturing Methods of Industry 4.0." *American Journal of Engineering and Applied Sciences* 16: 12-22. https://doi.org/10.3844/ajeassp.2023.12.22.

Kim, N. 2015. *Introduction to Nonlinear Finite Element Analysis*. 1st ed. New York: Springer. https://doi.org/10.1007/978-1-4419-1746-1.

Kizhakkinan, U., S. Seetharaman, N. Raghavan, and D. W. Rosen. 2023. "Laser Powder Bed Fusion Additive Manufacturing of Maraging Steel: A Review." *Journal of Manufacturing Science and Engineering* 145, no. 11: 110801. https://doi.org/10.1115/1.4062727.

Kosiba, K., T. Gustmann, J. T. Kim, J. Seok, J. Jung, L. Beyer, S. Scudino, L. Giebeler, J. Han, and J. K. Hufenbach. 2023. "Experimental Cooling Rates During High-Power Laser Powder Bed Fusion at Varying Processing Conditions." *Journal of Alloys and Compounds* 967: 171773. https://doi.org/10.1016/j.jallcom.2023.171773.

Koza, J. R. 1994. "Genetic Programming as a Means for Programming Computers by Natural Selection." *Statistics and Computing* 4, no. 2: 87-112. https://doi.org/10.1007/BF00175355.

Leirmo, T. S., and K. Martinsen. 2019. "Evolutionary Algorithms in Additive Manufacturing Systems: Discussion of Future Prospects." *Procedia CIRP* 81: 671-676. https://doi.org/10.1016/j.procir.2019.03.174.

Li, X., Y. Liu, C. Tan, and Y. Zou. 2023. "Porosity Formation Mechanisms, Microstructure Evolution and Mechanical Performance of AlMgScZr Alloy Fabricated by Laser Powder Bed Fusion: Effect of Hatch Distance." *Journal of Manufacturing Processes* 94: 107-119. https://doi.org/10.1016/j.jmapro.2023.03.047.

Liu, C., H. Gao, L. Li, J. Wang, C. Guo, and F. Jiang. 2021. "A Review on Metal Additive Manufacturing: Modeling and Application of Numerical Simulation for Heat and Mass Transfer and Microstructure Evolution." *China Foundry* 18, no. 4: 317-334. https://doi.org/10.1007/s41230-021-1119-2.

Liu, M., K. Wei, and X. Zeng. 2022. "High Power Laser Powder Bed Fusion of AlSi10Mg Alloy: Effect of Layer Thickness on Defect, Microstructure and Mechanical Property." *Materials Science and Engineering: A* 842: 143107. https://doi.org/10.1016/j.msea.2022.143107.

Lücke, T. G., L. Schüller, A. Vogelpoth, T. Laag, J. Saewe, and C. L. Häfner. 2023. "Influence of Laser Power and Scan Speed on the Formation of Hot Cracks During the Processing of High-Speed Steel HS2-2-2 by Laser Powder Bed Fusion." *BHM Berg- und Hüttenmännische Monatshefte* 168, no. 5: 239-246. https://doi.org/10.1007/s00501-023-01353-4.

Meng, G., J. Zhang, L. Zhu, Q. Lan, and Z. Jiang. 2023. "Effect of Process Optimization on Laser Additive Manufacturing of Inconel 718 Alloy Based on Finite Element Analysis: Thermal and Structural Evaluation." *Optics & Laser Technology* 162: 109261. https://doi.org/10.1016/j.optlastec.2023.109261.

Mugwagwa, L. 2016. *Residual Stresses and Distortions in Selective Laser Melting - A Review*.

Mugwagwa, L., D. Dimitrov, S. Matope, and I. Yadroitsev. 2018. "Influence of Process Parameters on Residual Stress Related Distortions in Selective Laser Melting." *Procedia Manufacturing* 21: 92-99. https://doi.org/10.1016/j.promfg.2018.02.099.

Mugwagwa, L. 2019. *Investigation and Management of Residual Stresses in Selective Laser Melting of Maraging Steel*. PhD diss., Stellenbosch University. http://hdl.handle.net/10019.1/105857.

Papazoglou, E. L., N. E. Karkalos, P. Karmiris-Obratański, and A. P. Markopoulos. 2022. "On the Modeling and Simulation of SLM and SLS for Metal and Polymer Powders: A Review." *Archives of Computational Methods in Engineering* 29, no. 2: 941-973. https://doi.org/10.1007/s11831-021-09601-x.

Parsazadeh, M., S. Sharma, and N. Dahotre. 2023. "Towards the Next Generation of Machine Learning Models in Additive Manufacturing: A Review of Process Dependent Material Evolution." *Progress in Materials Science* 135: 101102. https://doi.org/10.1016/j.pmatsci.2023.101102.

Paul, M. J., Y. Muniandy, J. J. Kruzic, U. Ramamurty, and B. Gludovatz. 2022. "Effect of Heat Treatment on the Strength and Fracture Resistance of a Laser Powder Bed Fusion-Processed 18Ni-300 Maraging Steel." *Materials Science and Engineering: A* 844: 143167. https://doi.org/10.1016/j.msea.2022.143167.

Pauzon, C., A. Leicht, U. Klement, P. Forêt, and E. Hryha. 2020. "Effect of the Process Gas and Scan Speed on the Properties and Productivity of Thin 316L Structures Produced by Laser-Powder Bed Fusion." *Metallurgical and Materials Transactions A* 51, no. 10: 5339-5350. https://doi.org/10.1007/s11661-020-05923-w.

Porter, S. C., R. Verseput, and C. R. Cunningham. 1997. "Process Optimization Using Design of Experiments." *Pharmaceutical Technology* 21: 60-70.

Rao, B. S., and T. B. Rao. 2022. "Effect of Process Parameters on Powder Bed Fusion Maraging Steel 300: A Review." *Lasers in Manufacturing and Materials Processing* 9, no. 3: 338-375. https://doi.org/10.1007/s40516-022-00182-6.

Rao, S. S. 2019. *Engineering Optimization Theory and Practice*. John Wiley & Sons, Inc. https://doi.org/10.1002/9781119454816.

Rautio, T., S. Ridal, M. Jaskari, A. Mustakangas, M. Hietala, and A. Järvenpää. 2023. "The Influence of Layer Thickness on the Fatigue Life of Laser Powder Bed Fusion Manufactured AlSi10Mg Parts." In *2023 4th International Conference on Industrial Engineering and Artificial Intelligence (IEAI)*, 94-98. Chiang Mai, Thailand, 2023. https://doi.ieeecomputersociety.org/10.1109/IEAI59107.2023.00021.

Roberts, M., M. Xia, and A. Kennedy. 2022. "Data-Driven Process Parameter Optimization for Laser Wire Metal Additive Manufacturing." In *2022 27th International Conference on Automation and Computing (ICAC)*, 1-6. Bristol, United Kingdom, 2022. https://doi.org/10.1109/ICAC55051.2022.9911139.

Rudolph, G. "Evolutionary Search under Partially Ordered Fitness Sets." 1999.

Shange, M., I. Yadroitsava, A. D. Plessis, and I. Yadroitsev. "Roughness and Near-Surface Porosity of Unsupported Overhangs Produced by High-Speed Laser Powder Bed Fusion." *3D Printing and Additive Manufacturing* 9, no. 4 (2021): 288–300. https://doi.org/10.1089/3dp.2020.0097.

Uçak, N., A. Çiçek, and K. Aslantas. "Machinability of 3D Printed Metallic Materials Fabricated by Selective Laser Melting and Electron Beam Melting: A Review." *Journal of Manufacturing Processes* 80 (2022): 414–457. https://doi.org/10.1016/j.jmapro.2022.06.023.

Will, J., and T. Most. *Metamodell of Optimized Prognosis (MoP): An Automatic Approach for User Friendly Parameter Optimization*. 2009. https://doi.org/10.13140/2.1.4946.9122.

Wohlers, T.T., R.I. Campbell, O. Diegel, R. Huff, J. Kowen, R. Newton, Wohlers Associates (Firm), J. Van Rensburg, C. Scott, and ASTM International. *Wohlers Report 2023: 3D Printing and Additive Manufacturing: Global State of the Industry*. Wohlers Associates, 2023. https://books.google.com.tr/books?id=4K3bzwEACAAJ.

Zhang, W., W. M. Abbott, A. Sasnauskas, and R. Lupoi. "Process Parameters Optimisation for Mitigating Residual Stress in Dual-Laser Beam Powder Bed Fusion Additive Manufacturing." *Metals* 12, no. 3 (2022): 420. https://doi.org/10.3390/met12030420.

Zhang, Z., S. Wang, H. Liu, L. Wang, and X. Xiao. "Effects of Hatch Distance on the Microstructure and Mechanical Anisotropy of 316 L Stainless Steel Fabricated by Laser Powder Bed Fusion." *Journal of Materials Engineering and Performance* 32, no. 10 (2023): 4757–4767.

Zhao, H., Z. Liu, C. Yu, C. Liu, and Y. Zhan. "Finite Element Analysis for Residual Stress of TC4/Inconel718 Functionally Gradient Materials Produced by Laser Additive Manufacturing." *Optics & Laser Technology* 152 (2022): 108146. https://doi.org/10.1016/j.optlastec.2022.108146.

Zienkiewicz, O. C., R. L. Taylor, and J. Z. Zhu. *The Finite Element Method: Its Basis and Fundamentals*. 6th ed. Oxford: Butterworth-Heinemann, 2005.

APPENDIX A

Table A.1. Thermal strain scaling factors calculated for each distinct simulation

Inputs				Outputs		
Layer thickness (μm)	Laser power (W)	Scanning speed (mm/s)	Thermal Strain Scaling Factor	Porosity (%)	Relative density (%)	Maximum deflection (mm)
30	80	400	1.7802	11.52	88.48	0.5
30	80	300	1.6538	9.02	90.98	0.39
30	80	200	0.0181	5.25	94.75	0.18
30	100	500	1.9084	3.96	96.04	0.74
30	100	400	1.7846	4.03	95.97	0.51
30	100	300	1.6421	8.97	91.03	0.33
30	120	500	2.0483	1.96	98.04	0.87
30	120	400	1.8326	3.47	95.63	0.65
30	120	300	1.6445	6.11	93.89	0.34
30	140	600	2.0946	1.23	98.77	0.89
30	140	500	2.0631	3.1	96.9	0.88
30	140	400	1.8703	3.73	96.27	0.71
30	160	700	2.5990	0.94	99.06	1.1
30	180	700	2.7506	0.65	99.35	1.16
30	160	600	2.4324	1.09	98.91	1.03
30	160	400	1.9552	3.41	96.59	0.81
30	160	300	1.7134	4.61	95.39	0.65
30	160	800	2.6818	3.65	96.35	1.13
30	180	800	2.7623	0.79	99.21	1.16
30	180	900	2.5778	1.23	97.77	1.09
30	180	1000	2.8202	1.53	98.47	1.18
30	180	600	2.4579	0.42	99.58	1.04

Cont. on next page

Table A.1. (cont.)

30	180	500	2.0482	1.38	98.62	0.87
30	180	400	1.7499	5.11	94.89	0.38
45	120	400	0.3673	9.58	90.42	0.2
45	120	300	0.3893	9.94	90.06	0.14
45	120	200	0.2779	10.24	89.76	0.25
45	120	500	0.2875	4.19	95.81	0.41
45	140	400	0.4009	9.41	90.59	0.13
45	140	300	0.4450	8.38	91.62	0.02
45	160	500	0.4105	4.14	95.86	0.12
45	160	400	0.4152	4.76	95.24	0.1
45	160	300	0.4496	8	92	0.01
45	180	600	0.2576	0.65	99.35	0.51
45	180	500	0.3225	1.52	98.48	0.3
45	180	400	0.4207	10.28	89.72	0.09
45	180	300	0.4221	7.09	92.91	0.07

APPENDIX B

Table B.1. Design points yielding deformations smaller than a micrometre

Inputs					Output
Design Point #	Layer thickness (μm)	Laser power (W)	Scanning speed (mm/s)	Thermal Strain Scaling Factor	Maximum deflection (mm)
156	45.00	149.105	251.122	1.4482	0.000963
163	45.00	146.542	253.871	1.4482	0.000421
182	45.00	149.609	251.122	1.4482	0.000991
220	45.00	146.784	253.871	1.4482	0.000308
221	45.00	146.784	253.871	1.4482	0.000308
223	45.00	146.636	253.871	1.4482	0.000376
226	45.00	152.121	253.871	1.4482	0.000631
232	45.00	146.883	253.871	1.4482	0.000265
243	45.00	146.824	253.871	1.4482	0.000291
244	45.00	146.695	253.871	1.4482	0.000349
247	45.00	146.068	253.871	1.4482	0.000676
248	45.00	152.560	253.871	1.4482	0.000897
249	45.00	151.489	253.871	1.4482	0.000312
253	45.00	146.790	253.871	1.4482	0.000306
254	45.00	146.819	253.871	1.4482	0.000293
262	45.00	146.817	253.871	1.4482	0.000293
265	45.00	146.912	253.871	1.4482	0.000253
272	**45.00**	**150.843**	**253.871**	**1.4482**	**0.000063**
273	45.00	146.884	253.871	1.4482	0.000265
279	45.00	146.530	253.871	1.4482	0.000428
285	45.00	151.252	253.871	1.4482	0.000211
287	45.00	146.911	253.871	1.4482	0.000253
288	45.00	146.884	253.871	1.4482	0.000265
290	45.00	150.251	253.871	1.4504	0.000782
294	45.00	147.371	253.871	1.4482	0.000079
295	45.00	151.506	253.871	1.4482	0.000319
300	45.00	150.843	253.871	1.4482	0.000063
303	45.00	151.252	253.871	1.4482	0.000211
310	45.00	151.252	252.493	1.4482	0.000808

Cont. on next page

Table B.1. (cont.)

315	45.00	148.839	252.625	1.4482	0.000319
319	45.00	151.299	252.493	1.4482	0.000828
328	45.00	147.371	252.625	1.4482	0.000596
329	45.00	146.650	252.493	1.4482	0.000936
330	45.00	152.149	253.871	1.4482	0.000647
350	45.00	147.371	253.871	1.4482	0.000079
376	45.00	147.371	253.871	1.4482	0.000079
379	45.00	147.371	253.871	1.4482	0.000079
399	45.00	150.843	253.871	1.4482	0.000063
405	45.00	147.371	253.871	1.4482	0.000079
406	45.00	150.843	253.871	1.4482	0.000063
413	45.00	147.371	252.295	1.4482	0.000734
420	45.00	150.843	253.871	1.4482	0.000063
423	45.00	145.982	253.871	1.4482	0.000727
433	45.00	145.636	253.871	1.4482	0.000945
438	45.00	146.325	253.871	1.4482	0.000533
441	45.00	147.371	253.871	1.4482	0.000079
443	45.00	150.843	253.871	1.4482	0.000063
457	45.00	148.453	251.859	1.4482	0.000679
477	45.00	147.371	251.859	1.4482	0.000919
478	45.00	151.824	253.871	1.4482	0.000472
479	45.00	150.862	252.343	1.4482	0.000729
156	45.00	149.105	251.122	1.4482	0.000963
163	45.00	146.542	253.871	1.4482	0.000421
182	45.00	149.609	251.122	1.4482	0.000991
220	45.00	146.784	253.871	1.4482	0.000308
221	45.00	146.784	253.871	1.4482	0.000308
223	45.00	146.636	253.871	1.4482	0.000376
226	45.00	152.121	253.871	1.4482	0.000631
232	45.00	146.883	253.871	1.4482	0.000265
243	45.00	146.824	253.871	1.4482	0.000291
244	45.00	146.695	253.871	1.4482	0.000349
247	45.00	146.068	253.871	1.4482	0.000676
248	45.00	152.560	253.871	1.4482	0.000897